Paleoceanography and Paleoclimatology

RESEARCH ARTICLE
10.1029/2020PA004019

Special Section:
The Arctic: An AGU Joint Special Collection

Holocene Interactions Between Glacier Retreat, Sea Ice Formation, and Atlantic Water Advection at the Inner Northeast Greenland Continental Shelf

Nicole Syring[1], Jeremy M. Lloyd[2], Ruediger Stein[1,3], Kirsten Fahl[1], Dave H. Roberts[2], Louise Callard[4], and Colm O'Cofaigh[2]

[1]Alfred Wegener Institute (AWI), Helmholtz Centre for Polar and Marine Research, Bremerhaven, Germany, [2]Department of Geography, Durham University, Durham, UK, [3]MARUM—Center for Marine Environmental Sciences and Faculty of Geosciences, University of Bremen, Bremen, Germany, [4]School of Geography, Politics and Sociology, Newcastle University, Newcastle upon Tyne, UK

Abstract During the past four decades significant decrease in Arctic sea ice and a dramatic ice mass loss of the Greenland Ice Sheet (GIS) has been coincident with global warming and an increase in atmospheric CO_2. In Northeast Greenland significant mass loss from the outlet glaciers Nioghalvfjerdsbræ (79NG) and Zachariæ Isstrøm (ZI) and intensive seasonal breakup of the local Norske Øer Ice Barrier (NØIB) have also been observed since 2000. In order to better understand the processes driving these modern changes, studies of paleoclimate records are important and of major societal relevance.
A multiproxy study including organic-biogeochemical and micropaleontological proxies was carried out on a marine sediment core recovered directly in front of 79NG. Data from Core PS100/270 evidenced a strong inflow of warm recirculating Atlantic Water across the Northeast Greenland shelf from the early Holocene between ~10 and 7.5 ka. An overall high in phytoplankton productivity occurred within a stable sea ice margin regime, accompanied by 79NG retreat most probably triggered by peak solar insolation and changes in the local ocean circulation. Enhanced basal melt of the underside of 79NG at ~7.5 ka then led to the total disintegration of the ice shelf. The released freshwater would have driven water column stratification and promoted the formation of the local landfast ice barrier, which is shown by lowered biomarker values and foraminifera abundances toward the end of the early Holocene. Near perennial sea ice conditions with short summers and 79NG retreat to the inner fjord then prevailed from ~7.5 to ~0.8 ka.

Key Points:

- Multiproxy record allowed reconstruction of NEG ice sheet retreat and sea ice history from the last deglaciation to the late Holocene
- Increased inflow of warm recirculating Atlantic Water linked to retreat and disintegration of the 79NG between 10 and 7.5 ka
- Extended to even perennial sea ice conditions were predominant on the inner NE Greenland shelf since 7.5 ka

Supporting Information:

- Figure S1
- Figure S2
- Figure S3

Correspondence to:
N. Syring,
nsyring@awi.de

Citation:
Syring, N., Lloyd, J. M., Stein, R., Fahl, K., Roberts, D. H., Callard, L., & O'Cofaigh, C. (2020). Holocene interactions between glacier retreat, sea ice formation, and Atlantic water advection at the inner Northeast Greenland continental shelf. *Paleoceanography and Paleoclimatology*, *35*, e2020PA004019. https://doi.org/10.1029/2020PA004019

Received 25 JUN 2020
Accepted 14 OCT 2020
Accepted article online 16 OCT 2020

1. Introduction and Regional Setting

In the past three decades, anthropogenic climate change has had a rapid and dramatic effect on Arctic sea ice and the Greenland Ice Sheet (Dai et al., 2019; Shepherd et al., 2020). The drastic increase of atmospheric CO_2 concentrations has led to rising ocean and atmosphere temperatures, which are compounded by Arctic amplification and complex positive feedback loops, for example, albedo feedback (Dai et al., 2019; Day et al., 2012; Kay et al., 2011; Notz & Marotzke, 2012; Thackeray & Hall, 2019). Both are key components of the climate system, while the strong negative shift in mass balance of GIS may cause a global sea-level rise of up to 0.09 to 0.88 m by the year 2100, causing irreversible damage to the environment and enormous economic impacts on our society (Meredith et al., 2019; Nordhaus, 2019; Stern & Taylor, 2007). GIS surface melt and its related accelerated mass loss coincided with a period of rapidly shrinking seasonal sea ice extent in the Arctic Ocean and surrounding marginal seas during the late 20th/early 21st century (Abdalati & Steffen, 2001; Comiso et al., 2008; Mote, 2007; Parkinson & Cavalieri, 2008; Stroeve et al., 2007; Tedesco, 2007). The main drivers of GIS mass change and observed Arctic summer sea ice loss are increased atmospheric temperatures and oceanic heat flux (Enderlin et al., 2014; Notz & Stroeve, 2016; Sasgen et al., 2012; van den Broeke et al., 2009). Changes in the dynamics of atmospheric temperatures and oceanic heat flux might lead to surface and bottom melt of ice sheets, the disintegration and speed up of marine-terminating outlet glaciers and ice streams, as well as thinning of multiyear sea ice and decreasing formation of first-year ice on the Siberian shelves (Holland et al., 2008; Krumpen et al., 2019; Maslanik et al., 2007; Nick et al., 2009; Rignot & Mouginot, 2012; Thomas et al., 2009). Recent satellite observations show that GIS mass loss and the Arctic sea ice loss have doubled since the beginning of this century (Kjeldsen et al., 2015).

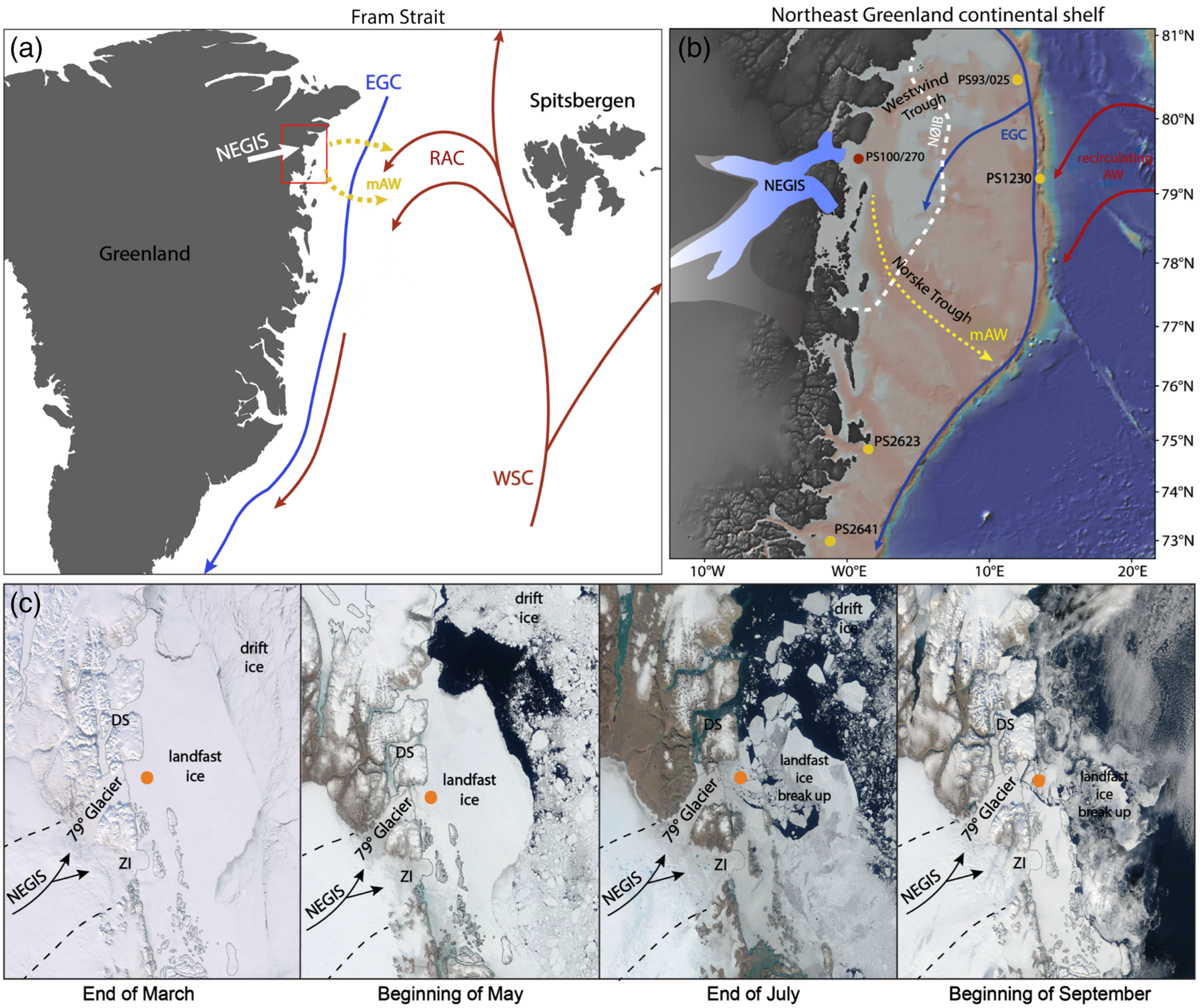

Figure 1. (a) Overview map of the Fram Strait, showing the main ocean currents: Warm West Spitsbergen current = WSC (red arrows), Return Atlantic Current (RAC), and the cold East Greenland current = EGC, modified recirculating Atlantic Water = mAW (yellow, dashed arrows) (map created with ODV, Schlitzer, 2018). Red rectangle marks the study area, including the Northeast Greenland ice stream = NEGIS (white arrow) and its marine-terminating outlet glaciers 79°N Glacier (79NG), Zachariæ Isstrøm (ZI). (b) Schematic map with characteristic features of the NEG continental shelf: EGC, NEGIS, Norske and Westwind troughs, Norske Øer ice barrier = NØIB, location of Core PS100/270 (this study, orange circle) and locations of other cores mentioned in the text (yellow dots) (map created with GeoMapApp, Ryan et al., 2009). (c) Modern seasonal sea ice conditions with a complete sea ice cover in March, the seasonal formation of the Northeast-Water Polynya = NEW Polynya in May and lowest sea ice extent in September (satellite images, NASA Worldview, 2019).

The Northeast Greenland Ice Stream (NEGIS) is one of the largest (700 km long) ice streams of GIS (Figures 1a and 1b) and interactions between its marine-terminating outlet glaciers, local sea ice formation, drift ice, and regional ocean dynamics influence and control environmental conditions on the Northeast Greenland (NEG) continental shelf (Figure 1c).

These parameters strongly depend on the incoming radiation, and atmospheric and ocean circulation and their dynamics affect climate on a regional and global scale by regulating heat and mass exchange between the ocean and atmosphere, surface albedo, primary production, deep-water formation, and sea-level rise (Arndt et al., 2015; Fahnestock et al., 1993).

NEGIS currently drains ~12% (320,000 km^2) of the GIS via three main outlet glaciers: Nioghalvfjerdsbræ (79NG), Zachariæ Isstrøm (ZI), and Storstrømmen with flow speeds up to >1 km/yr (Figure 1c; Khan et al., 2014; Larsen et al., 2018; Rignot & Mouginot, 2012). The drainage basins of 79NG and ZI hold ~1.1 m of sea level equivalent (Mouginot et al., 2015).

The study area is located to the east of the floating ice shelves of 79NG and ZI, which front NEGIS (Figure 1b). The total length of the floating ice tongue of 79NG is ~80 km and 21 km in width, with contemporary basal melt rates of 10.4 ± 3.1 m yr^{-1} (Joughin et al., 2001; Reeh et al., 2001; Schaffer et al., 2020). Until recently the northeast sector of the GIS was considered to be relatively stable compared to other regions of Greenland; however, this region is now seen to be more and more threatened by anthropogenic climate changes (Helm et al., 2014; Khan et al., 2014). Similar basal conditions occur at the ZI, although this glacier has experienced collapse and rapid retreat since 2002 (velocity has tripled) with the consequence of losing ~95% of its residual ice shelf (Khan et al., 2014; Mouginot et al., 2015; Rignot & Kanagaratnam, 2006). Concurrently, 79NG lost ~30% of its floating ice tongue and suffers from grounding-line retreat (2 km inland) between 1998 and 2014 (Mayer et al., 2018; Mouginot et al., 2015). Ice flow models, for example, by Choi et al. (2017) indicate that 79NG is less vulnerable than ZI due to its upward sloping bed close to the present ground line and a series of pinning points close to the calving front (Choi et al., 2017). Satellite-derived data suggest that ZI is actually at its tipping point and 79NG very close to it (Krieger et al., 2020; Mouginot et al., 2015, 2019).

Large supplies of freshwater originate from bottom melting of 79NG, comprising a freshwater volume ranging between 11 km^3 a^{-1} (0.4 mSv) and 30 km^3 a^{-1} (1.0 mSv), accounting for 4% and 13% of the recent freshwater loss from the GIS (Smedsrud et al., 2017). Recent observations show a rapid, active melting at 79NG grounding zone, resulting in a mass loss accompanied by a thinning of the ice margin, reduced ice shelf strength, and hence, a reduced buttressing effect (Rignot et al., 1997; Seroussi et al., 2011).

The East Greenland Current (EGC) carries Polar Water (PW, salinities less than 34.5‰, temperatures below 0°C) and drift ice from the interior of the Arctic Ocean southward along the NEG continental shelf, where it circulates anticlockwise through the Norske and Westwind Trough around the Belgica Bank (Figures 1a and 1b; Bourke & Garrett, 1987; Budéus & Schneider, 1995; Johnson & Niebauer, 1995; Topp & Johnson, 1997). Warmer recirculating Atlantic Water (AW) crosses the inner shelf from the east via the narrow and deep channels in the Norske and Westwind Troughs, which converge at a relatively shallow sill at their western end near the margin of the NEGIS ice shelf (Figure 1b; Mayer et al., 2000; Reeh et al., 2001; Schaffer et al., 2020; Straneo et al., 2012). AW mixes with the meltwater from the local glaciers and these glacially, less dense modified Atlantic Water (mAW, ~0.9°C cooler than inflowing AW) flows back and/or south along the Norske Trough (Schaffer et al., 2020).

The Norske Øer Ice Barrier (NØIB), an area of semipermanent fast-ice between 78–80°N, varies annually in size and thickness. This ice barrier stretches 75–150 km from the coast toward the middle of the shelf and is bordered by drift ice floating southward via the EGC (Figure 1c). The Northeast Water (NEW) Polynya, another important feature of the NEG continental shelf is located at the northern tip of NØIB (Figure 1c; Budéus et al., 1997). Two ice barriers support the seasonal formation of the NEW Polynya, the Ob Ice Barrier by pushing drift ice eastward while NØIB blocks the northward flowing sea ice which is entrained in the NEG Coastal Current (Schneider & Budéus, 1994). This reduces outlet glaciers calving into the EGC due to its buttressing effect (Figure 1c; Dupont & Alley, 2005; Reeh et al., 2001; Schneider & Budéus, 1994, 1997). Recent observations show that calving does not occur when the NØIB forms in front of the glaciers. When this occurs, the glacier itself advances slowly against the sea ice or pushes it ahead, but ice margin conditions basically do not change. Past studies indicate that since August 1997 the NØIB fast ice now regularly breaks up during late summer (every summer between 2002 and 2005), resulting in a significant and increased iceberg release from the floating ice tongues of 79NG and ZI, a rare event that previously probably took place only every ~50 years (Higgins, 1989, 1991; Hughes et al., 2011; Reeh et al., 2001). Perennial sea ice conditions of NØIB with 1 to 2 occasional break ups between 1982 and 2000 have changed from being a rare event to an annually recurring episodes and a predominately first year fast sea ice matrix after 2000 (Sneed & Hamilton, 2016). Reduced fast ice thickness, the presence of meltwater on the ice barrier and additionally melting due to warm AW pulses from below weakens the NØIB. Consequently, recent changes in NØIB stability might affect the dynamic of local currents, the NEW

Polynya and lead to increased flux of AW into the glacier cavity below 79NG (Hughes et al., 2011; Wilson & Straneo, 2015).

2. Aim of This Study

Recent studies have suggested that in Northeast Greenland the GIS advanced to the edge of the continental shelf during the Last Glacial Maximum (LGM) and retreated to the present coast by the beginning of the Holocene (11.5–9.0 ka; Arndt et al., 2015, 2017; Evans et al., 2009; Larsen et al., 2018; Winkelmann et al., 2010). Furthermore, there is evidence that 79NG and the ice shelf retreated up to 80 km inland during the early Holocene Thermal Maximum 10 to 8.0 ka (Bennike & Weideck, 2001) when high summer insolation increased atmospheric temperatures up to 4–5°C warmer than today and reduced sea ice concentration on the outer NEG continental shelf (Kaufman et al., 2004; Laskar et al., 2004; Reeh, 2004; Syring et al., 2020). However, the interaction between the ice sheet and its shelf dynamics and sea ice formation on the NEG shallow marine shelf system during the Holocene remains very poorly understood.

This study investigated a core record collected from the seafloor adjacent to the present 79NG shelf (Core PS100/270, Figure 1a), which records a history of proximal/distal glaciomarine and sub-ice shelf conditions as 79NG grounding line and ice shelf retreated passed this site during the LGM to Holocene recession. Critically, it also contains a record of sea ice conditions throughout the Holocene. In order to understand regional ice/ocean/climate feedbacks this record is compared with similar sedimentary records from the East Greenland continental shelf between 70° and 75°N (Evans et al., 2002; Nam et al., 1995; Stein, 2008; Stein et al., 1993). This study presents a multiproxy analysis based on specific biomarkers, organic bulk parameters, and benthic foraminifera data as summarized in Table 1. Based on these different proxies we aim to provide key insights into past sea ice formation, primary production of open-water phytoplankton, terrigenous input by vascular land plants, but also the influence of AW entering the inner NEG shelf, the timing of 79NG marine-terminating outlet glacier retreat and ice shelf disintegration during the Holocene. Furthermore, these data are related to sea ice settings as recorded by nearby core PS93/025 from the outer NEG and East Greenland records, for example, PS2623 and PS2641 from the inner continental shelf (Kolling et al., 2017; Stein, 2008; Syring et al., 2020).

3. Material and Methods

3.1. Material

Gravity Core PS100/270 was recovered aboard the RV Polarstern cruise PS100 in 2016 close to the floating ice tongue of 79NG on the inner NEG continental shelf (79°29.83′N, 18°8.40′W; 424 m water depth, Figure 1b; Kanzow, 2017). This core was selected and studied in detail to reconstruct past sea ice formation, terrigenous input, primary productivity, and the influence of warm AW on the shelf, using biomarker, bulk parameter and microfossil proxy data. The total core length of Core PS100/270 is 9.51 m. Once retrieved the core was split, photographed, and described on board, then wrapped in film and stored in plastic tubes at 4°C. A total of 162 subsamples were subsequently collected and stored at −20°C to prevent biomarker degradation prior to lipid extraction. The first 95 cm of the Core PS100/270 were sampled every 2 cm and afterward every ~8 cm. These samples were freeze dried and ground.

3.2. Methods

3.2.1. Physical Properties and Lithostratigraphy

Once split the cores were immediately described and information on grain size, sedimentary structures, sediment color, sorting, bed contacts, clast abundance, and macrofossil content was recorded. Additional information on sedimentary structures was provided postcruise from x-radiographs of the split core sections produced from a GEOTEK XCT scanner. Based on these data sets a lithostratigraphic log (including main lithofacies units) was produced (Figure 3). Magnetic susceptibility and wet bulk density were measured on split 1 m sections of the core using a GEOTEK Multi-Sensor Core Logger (MSCL).

3.2.2. Total Organic Carbon and Carbonate

Concentrations for total organic carbon (TOC) were determined on 162 subsamples with a Carbon-Sulfur Analyzer (CS-125, Leco) after removing any carbonate by adding hydrochloric acid to a 0.1 g subsample. Twenty milligrams of the sediment was used for total carbon (TC) and total nitrogen (TN) measurements, which were performed with a Carbon-Nitrogen-Sulfur Analyzer (Elementar III, Vario). Based on

Table 1
Overview of Investigated Biomarker and Micropaleontological Proxies Origin and Interpretations

Proxy	Source	Interpretation/comments	References
IP_{25} & HBI II	IP_{25}: sea ice associated pennate diatom (certain species of the genus *Pleurosigma* and *Haslea* spp.) HBI II: certain sympagic diatoms (e.g. *Berkeleya rutilans*)	source-specific, sensitive, and stable proxy seasonal Arctic spring sea ice cover (late Miocene to Holocene) combination with pelagic phytoplankton marker allows to distinguish between sea ice conditions (e.g., seasonal vs. perennial) ➔ PIP_{25} index	Belt et al. (2007, 2015, 2016) Brown et al. (2014) Müller et al. (2009, 2011, 2012) Fahl and Stein (2012) Stein et al. (2016) Köseoğlu, Belt, Husum, and Knies (2018), Köseoğlu, Belt, Smik, et al. (2018) Limoges et al. (2018) Reviews by Stein and Fahl (2012) Belt and Müller (2013) Belt (2018)
HBI III	pelagic diatoms (e.g., *Rhizosolenia setigera*) often abundant in spring MIZ phytoplankton bloom	pelagic productivity may reflect Marginal Ice Zone (MIZ) conditions	Smik et al. (2016) Belt et al. (2017) Ribeiro et al. (2017) Stein et al. (2017) Xiao et al. (2017)
Brassicasterol	biosynthesized by a broad marine/fluvial algae group	open-water (pelagic) productivity proxy is limited in regions influenced by strong riverine input for example the Siberian shelves (Kara and Laptev Sea)	Yunker et al. (1995) Volkman et al. (2008) Jaffé et al. (1995) Fahl et al. (2003) Belt and Müller (2013)
Dinosterol	predominantly by Dinoflagellates detected in minor amounts in sea ice and diatom cultures (*Navicula* spp.)	open-water (pelagic) productivity	Review by Volkman (1986) Volkman et al. (1993)
Campesterol & β-sitosterol	main producer are vascular land plants found in many diatoms	terrigenous input	Rontani et al. (2014) Fahl and Stein (2007)
Foraminifera shell	Foraminifera	planktic foraminifera: surface water productivity, temperature benthic foraminifera: water-mass characteristics (e.g., Atlantic Water inflow)	e.g. Hald and Korsun (1997); Jennings et al. (2011); Perner et al. (2015)

these bulk parameters TOC and TC, the carbonate ($CaCO_3$) content (130 samples) was calculated by $CaCO_3 = (TC–TOC) \times 8.333$ (8.333 as stoichiometric factor), assuming that calcite is the predominant carbonate phase.

3.2.3. Lipid Biomarker Extraction and Analysis

Specific highly branched isoprenoids (HBIs), including IP_{25}, HBI II diene, and HBI III (e and z) (159 subsamples) and certain type sterols (156 subsamples) brassicasterol (24-methylcholesta-5,22-dien-3β-ol) and dinosterol (4 α,23,24-Trimethyl-5α-cholest-22E-en-3β-ol), as well as β-sitosterol (24-ethylcholest-5-en-3β-ol) and campesterol (24-methylcholest-5en-3β-ol) were extracted to facilitate climate reconstructions. Internal standards 7-hexylnonadecane (7-HND, 0.076 μg/sample), 9-octylheptadec-8-ene (9-OHD, 0.1 μg/sample), 5α-androstan-3β-ol (androstanol, 10.7 μg/sample), and squalane (3.2 μg/sample) for the quantification of lipid biomarkers in each sample were added to 5 g of freeze-dried and homogenized sediment material. For the extraction, dichloromethane/methanol (DCM/MeOH, 2:1 *v*/v) was added to the sediment samples, followed by ultrasonification (15 min) and centrifugation (3 min) three times. Subsequently, we separated the hydrocarbon fraction (5 ml *n*-hexane) from the sterol fraction (9 ml ethylacetate/*n*-hexane) by open silica gel column chromatography. Finally, the sterol fraction was silylated by adding 200 μl of BSTFA (bis-trimethylsilyl-trifluoroacet-amide) at 60°C for 2 hr. Two different gas chromatography-mass spectrometers (GC-MS) with similar basic configuration were used to measure the extracted samples. The hydrocarbon fraction was measured with a gas chromatograph Agilent Technologies 7890B GC system (30 m DB-1MS column, 0.25 mm i.d., 0.25 μm film thickness) coupled to a mass spectrometer Agilent 5977A MSD (70 eV constant ionization potential, Scan 50–550 *m/z*, 1 scan/s, ion source temperature 230°C, Performance Turbo Pump) with the temperature program: 60°C (3 min), 150°C (heating rate: 15°C/min), 320°C (heating rate: 10°C/min), and 320°C (15 min, isothermal). The sterols were measured with a GC Agilent 6,850 GC coupled to an Agilent 5975C VL MSD (conditions see above) with the temperature sequence: 60°C (2 min), then 150°C (heating rate: 15°C/min), 320°C (heating rate: 3°C/min), and 320°C (20 min isothermal).

Component assignment was based on comparison of GC retention times with those of reference compounds and published mass spectra (sterols: Boon et al., 1979; Volkman, 1986; HBIs: Belt et al., 2007; Brown & Belt, 2016). The concentration of each biomarker was calculated by setting its individual GC-MS ion responses in relation to those of respective internal standards. For the quantification of the sterols (quantified as trimethylsilyl ethers), the molecular ions *m/z* 470 for brassicasterol, *m/z* 472 for campesterol, *m/z* 486 for β-sitosterol, and *m/z* 500 for dinosterol were used in relation to the molecular ion *m/z* 348 of the internal standard androstanol. For the quantification of IP_{25}, HBI II, and HBI III, their molecular ions (*m/z* 350 for IP_{25}, *m/z* 348 for HBI II, and *m/z* 346 for HBI III) were compared to the fragment ion *m/z* 266 of the internal standard 7-HND. The different responses of these ions were balanced by an external calibration. For further details we refer to Fahl and Stein (2012), Brown et al. (2014), and Belt (2018).

The calculated Kovats Index for IP_{25} is 2,085, for HBI II 2,084, and 2,046 for HBI III. All biomarkers of this study were normalized against the amount of sediment and TOC content. In order to distinguish between different sea ice settings IP_{25} was combined with open-water phytoplankton biomarkers (see Table 1), resulting in the so-called "PIP_{25} index" (Müller et al., 2011; Smik et al., 2016). We calculated the PIP_{25} indices according to the equation by Müller et al. (2011), where *c* is a concentration balance factor (to account for concentration differences between IP_{25} and phytoplankton biomarkers (P), that is., brassicasterol, dinosterol, or HBI III (z-isomer):

$$PIP_{25} = \frac{[IP_{25}]}{([IP_{25}] + c[P])} \text{ with } c = \frac{\text{mean}[IP_{25}]}{\text{mean}[P]} \tag{1}$$

The HBI II and a second form of HBI III (e-isomer), also proposed as proxies for sea ice and productivity reconstructions (see Belt, 2018; Belt, 2019), were determined but not presented and discussed in this paper. However, these data are available online under doi: 10.1594/PANGAEA.921185.

Biomarker concentrations were converted into accumulation rates by using the following equations (e.g., Stein & Macdonald, 2004):

$$\begin{aligned}
&(1)\ \text{TSAR} = \text{LSR} * (\text{WBD} - 1.026\,\text{PO}/100)\\
&(2)\text{TOCAR} = \text{TSAR} * \text{TOC}/100\\
&\quad \text{CaCO}_3\text{AR} = \text{TSAR} * \text{CaCO}_3/100\\
&\quad \text{BMAR} = \text{TSAR} * \text{BM}
\end{aligned}$$

$\text{LSR} = \text{sedimentation rate}\left(\text{cm kyr}^{-1}\right)$

$\text{WBD} = \text{wet bulk density}\ (\text{g cm}^{-3})$

$\text{TOC} = \text{total organic carbon}(\%)$

$\text{BM} = \text{biomarker concetration}\ (\mu\text{g g}^{-1}\ \text{Sed})$

$\text{PO} = \text{porosity}(\%)$

$\text{TSAR} = \text{total sediments accumulation rate}\left(\text{g cm}^{-2}\ \text{kyr}^{-1}\right)$

$\text{TOCAR} = \text{total organic carbon accumulation rate}\ \left(\text{g cm}^{-2}\ \text{kyr}^{-1}\right)$

$\text{CaCO}_3\text{AR} = \text{carbonate accumulationrate}\left(\text{g cm}^{-2}\ \text{kyr}^{-1}\right)$

$\text{BMAR} = \text{biomarkaer accumulation rate}\ \left(\mu\text{g cm}^{-2}\ \text{kyr}^{-1}\right)$

3.2.3.1. Foraminiferal Analysis

A total of 31 subsamples were collected for foraminiferal analysis, sampled at ~10 cm intervals for the first 100 cm, then every 32 cm down to a core depth of 450 cm, then every 64 cm to the base of the core. Sample volume varied between 0.5 and 5 ml (cm^3) depending on average foraminiferal concentration (estimated based on initial scanning of samples). The variation in sample size was designed to allow ~300 to 500

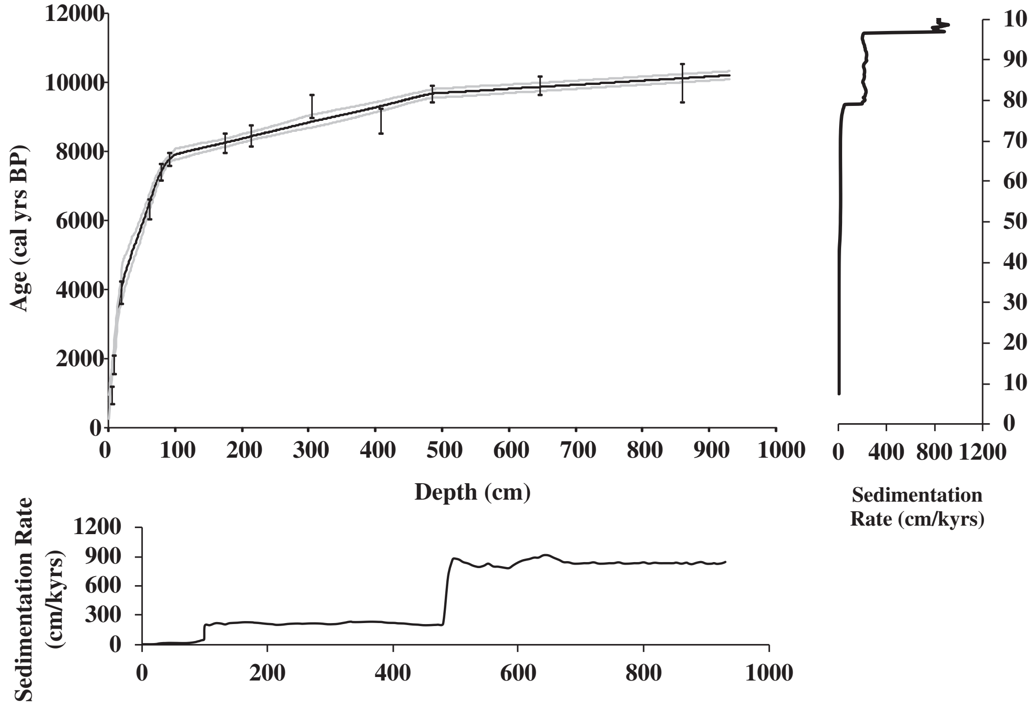

Figure 2. Age versus depth profile for Core PS100/270 including calibrated radiocarbon dates (Table 2) used for age model reconstructions (left) and sedimentations rates against age (right) and depth (below).

specimens to be counted from all samples. Once extracted samples were soaked in deionized water for several hours to help disaggregate the sediment. Samples were then washed through a 500 μm and 63 μm mesh sieve to concentrate the foraminifera. The material collected on the 63 μm mesh sieve was retained for foraminiferal analysis. Foraminifera were identified and counted from the wet residue under a binocular microscope straight away. Counting the foraminifera before drying reduced damage to agglutinated specimens and also smaller fragile calcareous species.

Samples were counted immediately to prevent dissolution of smaller fragile calcareous specimens. Once counted samples were air dried to preserve the material for further analysis.

Accumulation rates of foraminifera (FAR as individuals $\text{cm}^{-2}\ \text{ky}^{-1}$) were calculated following Ehrmann and Thiede (1985):

$$\text{FAR} = \text{TSAR}^{*}\text{FN},$$

where TSAR is the total sediment accumulation rate ($\text{g cm}^{-2}\ \text{kyr}^{-1}$) and FN the foraminifera number (individuals per gram sediment).

4. Results

4.1. Age Model of Core PS100/270 and Sedimentation Rates

The core chronology is based on 13 accelerator mass spectrometry (AMS) ^{14}C ages (Figure 2, Table 2) measured on mixed benthic foraminifera and a well-preserved articulated bivalve (*Yoldia* sp.) found at 480–484 cm. In addition, 5 ^{14}C AMS ages were also measured from planktic foraminifera (Table 2). Although the planktic foraminifera AMS dates were not used in generating the age model, there is a high degree of correlation between the planktic and mixed benthic foraminiferal ages (Table 2). This indicates very little difference in age of surface and deep waters on the continental shelf of NEG. AMS ^{14}C dating was carried out at the Alfred Wegener Institute Bremerhaven using the Mini Carbon Dating System (MICADAS) and through the UK NERC AMS radiocarbon facility. Radiocarbon ages were converted to calibrated calendar years before present (cal. years BP) using the calibration software CALIB 7.1 (Stuiver

Table 2
AMS^{14}C Radio Carbon Ages for GC PS100/270 Were Determined on Articulated Bivalve and Mixed Benthic/Planktic Foraminifers

Lab-ID	Depth (cm)	Material	AMS 14CAMS 14C	Error ±	CALIB median	CALIB min.	CALIB max.
AWI 4345.1.1	3–4	mixed benth. Foram.	1,483	59	**1,129**	883	1,297
AWI 4346.1.1	6–7	mixed benth. Foram.	2,339	62	**1,700**	1,558	1,890
AWI 4347.1.1	17–18	mixed benth. Foram.	4,051	67	**3,744**	3,420	3,989
AWI 4348.1.1	59–60	mixed benth. Foram.	6,028	75	**6,360**	6,149	6,614
AWI 4349.1.1	77–78	mixed benth. Foram.	7,020	79	**7,332**	7,190	7,488
UCIAMS-211080	88–92	mixed benth. Foram.	7,440	40	**7,691**	7,583	7,808
AWI 4350.1.1	170–175	mixed benth. Foram.	7,928	83	**8,234**	8,117	8,352
AWI 4351.1.1	210–215	mixed benth. Foram.	8,118	85	**8,424**	8,310	8,547
AWI 4352.1.1	300–304	mixed benth. Foram.	8,849	88	**8,845**	8,680	9,042
AWI 4353.1.1	404–408	mixed benth. Foram.	8,500	85	**9,298**	9,158	9,447
UCIAMS-211061	480–484	mixed benth. Foram.	9,145	50	**9,663**	9,542	9,786
UCIAMS-211081	644.5–645	bivalve	9,345	45	**9,869**	9,744	9,988
AWI 2795.1.1	856	mixed benth. Foram.	9,437	104	**10,123**	10,005	10,241
AWI 4354.1.1	3–4	mixed plankt. Foram.	1,434	58			
AWI 4355.1.1	6–7	mixed plankt. Foram.	2,198	63			
AWI 4356.1.1	17–18	mixed plankt. Foram.	3,702	68			
AWI 4357.1.1	59–60	mixed plankt. Foram.	6,024	79			
AWI 4358.1.1	210–215	mixed plankt. Foram.	7,799	86			

Note. Bold CALIB median numbers were used for our *Bacon* age model. AMS^{14}C ages in gray are from planktic foraminifera, which were excluded from further age calibrations due to the high correlation with benthic foraminifera.

et al., 2019) and the Marine13 curve (Reimer et al., 2013), and no additional local reservoir age correction was applied ($\Delta R = 150$; Larsen et al., 2018). The Bayesian accumulation age-depth modeling program, *Bacon 2.2* (Blaauw & Christen, 2011) was used to create a suitable age model for Core PS100/270 (Figure 2). Due to the coring process (gravity core) the surface sediments will not have been recovered (Parker & Sills, 1990). The age model generated using the *Bacon 2.2* program estimates a surface age of the gravity core of ~0.75 ka (indicating the last 750 years of sedimentation has been lost through the coring process). This explains the lack of data from the last 800 years from our record. The Bacon software was not forced to run to present as it is clear that sediment is missing from the top of the core. Calculated sedimentation rates vary significantly through the core. The bottom section between 930 to 470 cm shows high sedimentation rates of up to 900 cm kyr^{-1}, followed by an abrupt decrease to relatively stable values of ~200 cm kyr^{-1} until 95 cm. There is then a further decrease to relatively low sedimentation rates from 95 cm to the surface of <50 cm kyr^{-1} (Figure 2).

4.2. Lithofacies and Bulk Organic Parameters

Based on sediment composition changes and X-ray images, the sedimentary sequence in Core PS100/270 can be divided into four lithofacies units (LF1–4), which are explained in detail below (Figure 3). Sedimentology, organic bulk parameters, that is, TOC (%) and $CaCO_3$ (wt.%) and the physical properties such as magnetic susceptibility (MS, 10^6 Sl) and wet bulk density (WBD, g cm^{-3}), are plotted against depth (Figure 3).

LF1 represents a stiff, overconsolidated diamicton at the bottom of the core between 930 and 910 cm that consists of a massive dark reddish to gray sandy silt matrix with abundant large black subangular, subrounded clasts (<5 cm), and a fining upward trend. It is intercalated with color banded silty clay, containing granule to gravel size clasts (Figure 3). This diamicton is characterized by low values of TOC (<0.1%), $CaCO_3$ (8 wt.%), and MS (~800 10^6 Sl), but high WBD values (~2.4 g cm^{-3}). Accumulation rates of TOC, $CaCO_3$, and biomarkers cannot be calculated for this unit (Figure S1 in the supporting information).

LF2 between 910 and 490 cm represents a transition from a stiffer diamicton to an indistinct, irregular, partly laminated silty clay (Figure 3). This unit shows relatively moderate, but slightly increased TOC (~0.2% to 0.15%) and $CaCO_3$ (16 to 20 wt.%) content, and higher MS values (~1,800·10^6 Sl). This unit is also characterized by a significant reduction in WBD (down to 1.6 g cm^{-3}) (Figure 3). This interval occasionally contains fine silty layers and/or lenses and is intercalated with diamicton horizons at 820 and 740 cm, where most of

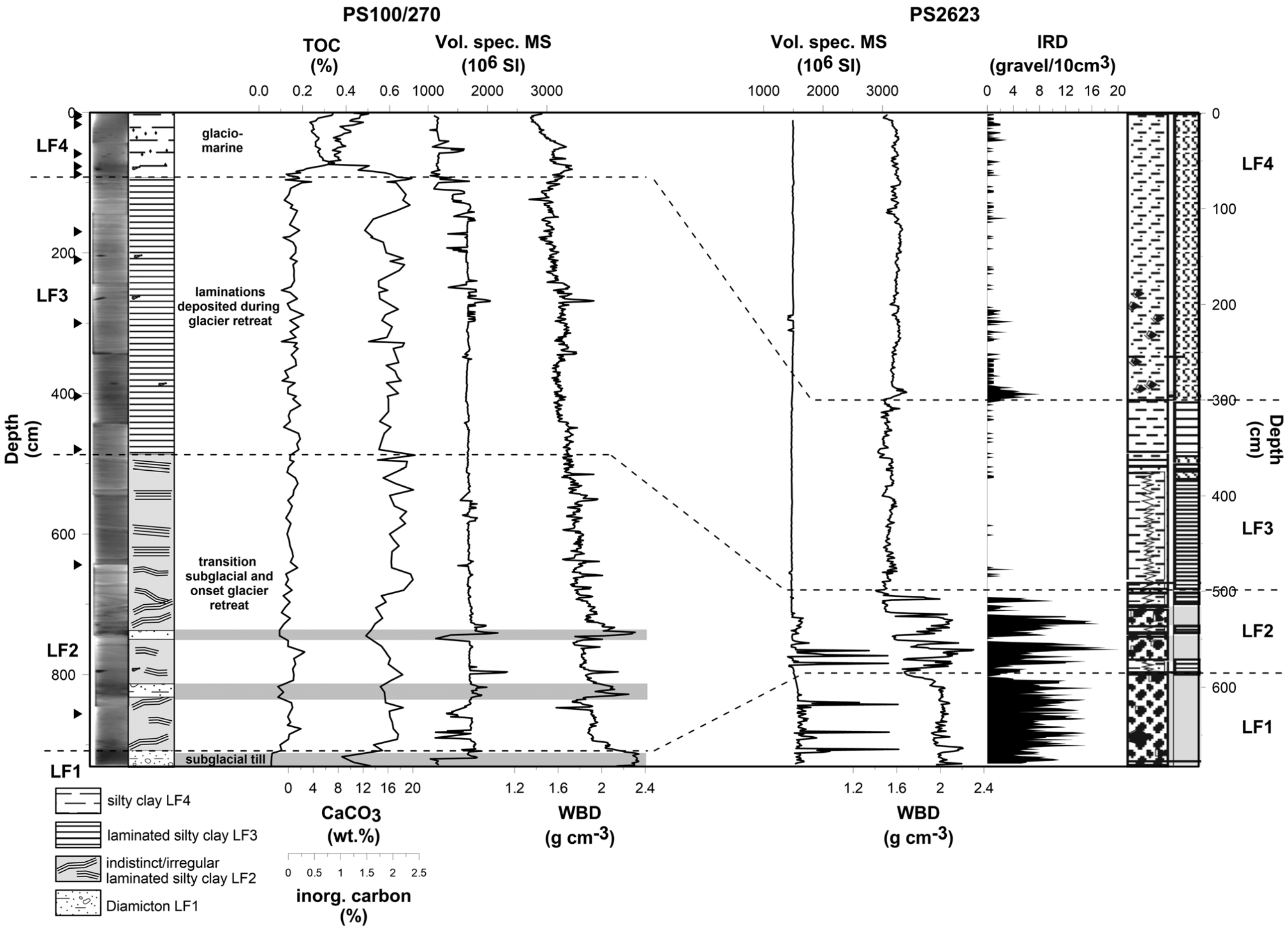

Figure 3. X-ray image and main lithology with lithofacies units LF1 to LF4 and interpreted depositional environment, and records of total organic carbon (TOC (%), $CaCO_3$ (wt. %), and physical properties (MS (10^6 Sl), WDB (g cm^{-3})), from GC PS100/270 (black lines) (this study). Gray shading indicates the basal diamicton and two intercalated diamicton horizons at 820 and 740 cm. Black triangles mark position of corrected ^{14}C AMS dates. To the right is the record from Core PS2623 (East Greenland, south of Shannon island) illustrating lithofacies, together with records of physical properties (MS [10^6 Sl], WDB [g cm^{-3}]) and ice-rafted debris (IRD (gravel 10 cm^{-3}) (Stein, 2008, and further references therein). Dashed lines show potential correlations between the cores.

the bulk parameters and physical properties, except for the WBD that shows distinct maxima, drop back to very low values (Figure 3). However, accumulation rates of TOC (up to 2.5 g cm^2 kyr^{-1}) and $CaCO_3$ (up to 300 g cm^2 kyr^{-1}) are highest in LF2 (Figures S1b and S1c in the supporting information).

LF3 (490 to 95 cm) predominately consists of strongly laminated reddish to gray/brown silty clays ranging between <1 cm and a few cm with rare black granule clasts. The upper part of this unit (130 to 95 cm), is characterized by a gradual transition from strongly laminated to homogenous silty clay (Figure 3). TOC (0.1%), $CaCO_3$ (18 to 20 wt.%), and MS (1,600 10^6 Sl) are all relatively constant and show only minor fluctuations while the WBD (down to 1.6 g cm^{-3}) is further decreasing (Figure 3). Accumulation rates of TOC (~0.25 g cm^2 kyr^{-1}) and $CaCO_3$ (~30 g cm^2 kyr^{-1}) are significantly decreased during this interval.

The final unit, LF4, comprising the upper part of the core between 95 to 0 cm, consists of very soft, but massive brownish silty clay to clay with occasional granule to gravel-sized clasts visible from 32 cm onward (Figure 3). TOC (0.5%) values increase and all other parameters, including $CaCO_3$ (4 wt.%), MS (~1,000 10^6 Sl), and WDB (1.4 g cm^{-3}) decrease through this unit (Figure 3). The unit LF4 is characterized by minimum TOC and $CaCO_3$ accumulation rates (Figures S1b and S1c).

4.3. Biomarkers

The biomarker data of LF1 (diamicton) are limited to two samples. The diamicton is characterized by low values of all HBIs; IP_{25} (0.4 μg g^{-1} TOC), HBI III (~0.25 μg g^{-1} TOC) (Figure 4). Phytoplankton

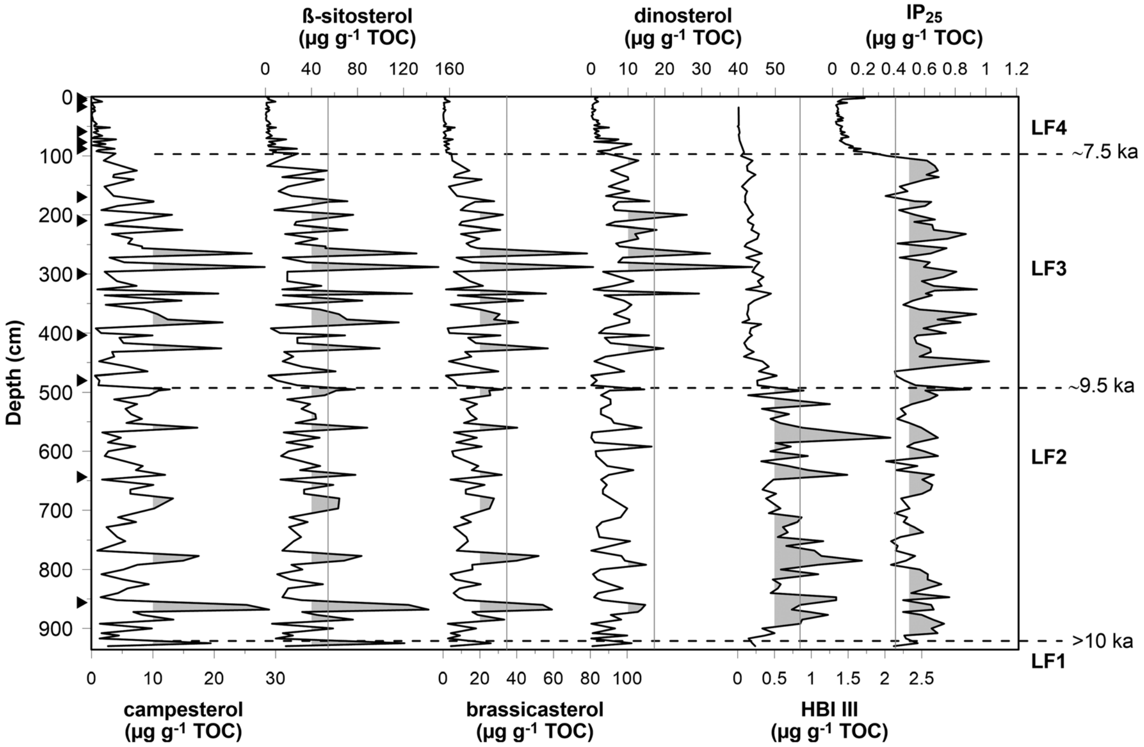

Figure 4. Lipid biomarker concentrations (μg g^{-1} TOC), including terrigenous biomarkers ß-sitosterol and campesterol, phytoplankton biomarkers brassicasterol, dinosterol and HBI III, and sea ice associated biomarker IP$_{25}$ against depth (cm). Gray-shaded areas highlight maxima of these records. Black triangles mark position of corrected ^{14}C AMS dates.

biomarkers brassicasterol (25 μg g^{-1} TOC) and dinosterol (10 μg g^{-1} TOC), but also terrigenous biomarkers ß-sitosterol (120 μg g^{-1} TOC) and campesterol (20 μg g^{-1} TOC) are somewhat higher during this interval (Figure 4). LF2 is characterized by strongly fluctuating, but overall high concentrations of all HBIs, that is, IP$_{25}$ (0.4 to 0.9 μg g^{-1} TOC), HBI III (0.5 to 2 μg g^{-1} TOC), and the sterols brassicasterol (10 to 60 μg g^{-1} TOC) and dinosterol (2 to 15 μg g^{-1} TOC), ß-sitosterol (40 to 160 μg g^{-1} TOC), campesterol (5 to 30 μg g^{-1} TOC), (Figure 4). Highest biomarker accumulation rates (Figure S1a to S1i) with strong fluctuations occur during LF2: sea ice associated biomarker IP$_{25}$ (ranging between 1 to 1.6 μg cm^2 kyr^{-1}), pelagic producers HBI III (up to 3 μg cm^2 kyr^{-1}), dinosterol (up to 160 μg cm^2 kyr^{-1}), and brassicasterol (up to 100 μg cm^2 kyr^{-1}), and terrigenous biomarker (up to 300 μg cm^2 kyr^{-1}, Figures S1d to S1i). In LF3 lipid biomarkers indicate similar strongly fluctuating trends with distinct peaks as in LF2, except for HBI III, which strongly decrease ~490 cm (down to 0.3 μg g^{-1} TOC) (Figure 4). Strongly fluctuating trends, but overall much lowered accumulation rates of all biomarkers are displayed in LF3, that is, IP$_{25}$ (~0.2 μg cm^2 kyr^{-1}), HBI III (0.2 μg cm^2 kyr^{-1}), dinosterol (~25 μg cm^2 kyr^{-1}), brassicasterol (~15 μg cm^2 kyr^{-1}), and terrigenous biomarker (~25 μg cm^2 kyr^{-1}) (Figures S1 d to S1i). The upper 95 cm show minimum lipid biomarkers concentrations and accumulation rates (Figure S1d to S1i). Concentrations of HBI III were below detection limit and showed no results during the upper ~100 cm.

4.4. Foraminifera

A total of 35 calcareous and 12 agglutinated benthic foraminiferal species were identified from the samples counted (Figure 5). The abundance of agglutinated specimens was generally very low (no single species having a relative abundance greater than 1% in any sample). Selected benthic foraminiferal species and planktic foraminiferal abundance are plotted for Core PS100–270 against depth in Figure 5. Absolute abundance of foraminifera varies from a minimum of 0 (sample at 928 cm) up to a maximum of 860 specimens per ml. Abundance of planktic specimens tracks that of benthic specimens but is approximately an order of magnitude lower.

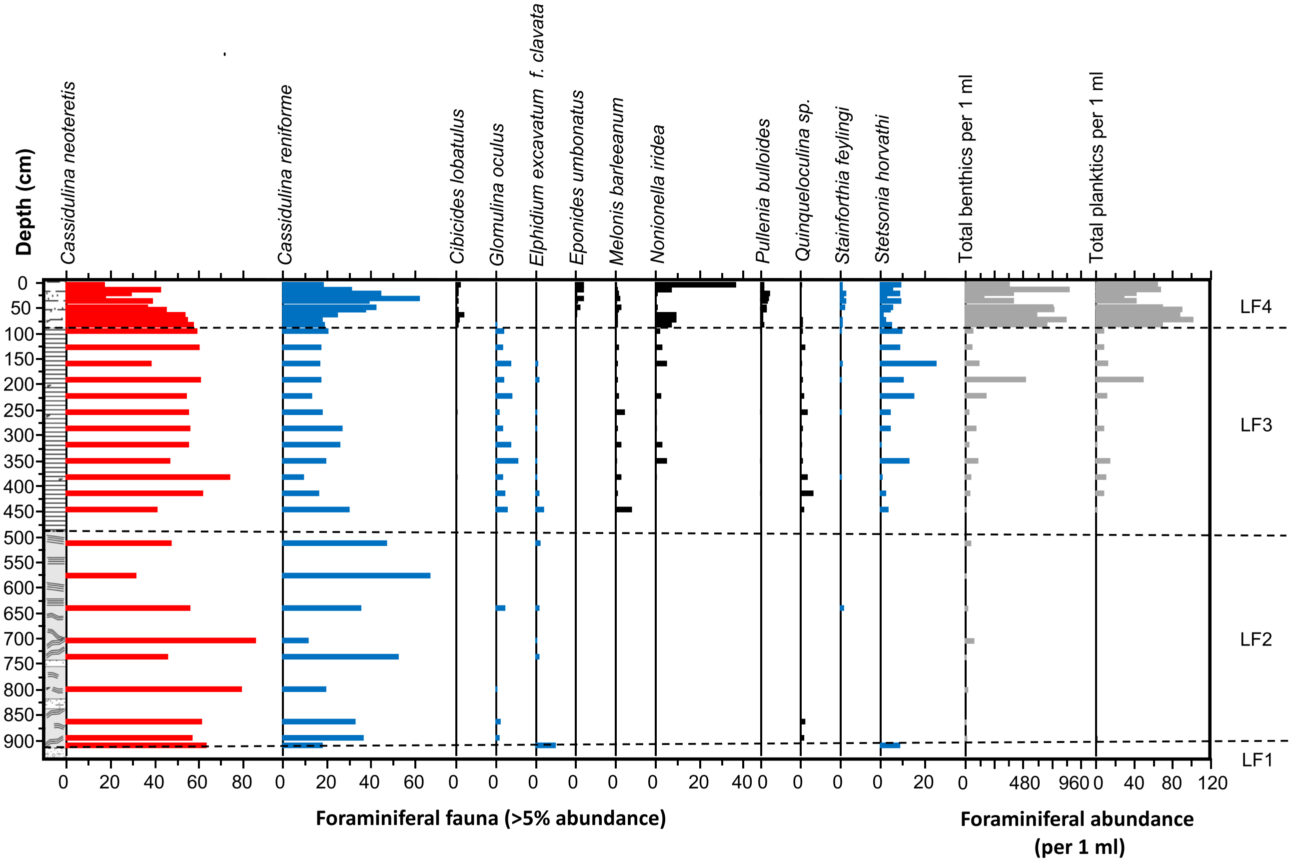

Figure 5. Foraminiferal assemblage of Core PS100/270 plotted against depth (cm), including only planktic and benthic species with an abundance ≥5%. *Cassidulina neoretetis* characterizes warm Atlantic water and *Cassiduline reniforme* cold polar water advection on the inner shelf. The major lithofacies types LF1 to LF4 are indicated (cf. Figure 3).

The diamicton (LF1) at the base of the core (930–910 cm) is barren of foraminifera (Figure 5) and therefore accumulation rates cannot not be calculated for this unit. The overlying weakly laminated silty clay LF2 unit (910–490 cm) is characterized by a low diversity and sparse fauna with absolute abundance below 30 specimens per ml of sediment (Figure 5).

The impoverished fauna is dominated by *Cassidulina neoteretis* (50–80%) with *Cassidulina reniforme* also abundant (20–40%). The transition to LF3 (the strongly laminated silty clays, 490–95 cm) is accompanied by a gradual increase in foraminiferal abundance (Figure 5). Accumulation rates of benthic foraminifera are highest through LF2 with 10,000–30,000 indiv. cm^{-2} kyr^{-1} and two extreme maxima of 45,000 and 60,000 indiv. cm^{-2} kyr^{-1} in LF2 and LF3, respectively, while the range of planktic foraminifera remains much lower (between 6,000 to 2,000 indiv. cm^{-2} kyr^{-1}), but also show highest contents during these intervals (Figure S1j and S1k). Abundance is initially relatively low, varying between 10 and 100 specimens per ml, then starts to increase from ~200 cm. LF3 is codominated by *C. neoteretis* and *C. reniforme* with dominance fluctuating between these two species (Figure 5). The accumulation rates of both species *C. neoteretis* (5,000 to 50,000 indiv. cm^{-2} kyr^{-1}) and *C. reniforme* (about 3,000 to 10,000 indiv. cm^{-2} kyr^{-1}) also reach highest levels during LF2 and LF3 (see discussion below).

From ~490 cm abundance of *C. reniforme* decreases to stabilize at ~20% with *C. neoteretis* returning to dominance (~60%). This interval is also characterized by the increase in abundance of other subsidiary species (Figure 5).

The transition to the upper massive silty clay LF4 unit at 95 cm is accompanied by an abrupt increase in foraminiferal abundance (up to 850 specimens per ml). Initially *C. neoteretis* continues to dominate, but the abundance of *C. reniforme* gradually increases reaching a peak abundance of 60% at 30 cm before reducing toward the top of the core as *C. neoteretis* increases slightly along with a range of other species, particularly *Nonionella iridea* (Figure 5). Accumulation rates of benthic (down to 1,000 indiv. cm^{-2} ky^{-1}) and planktic (near zero values) foraminifera are lowest in LF4, a similar pattern as recorded by the organic bulk parameters and lipid biomarkers (Figures S1j and S1k).

5. Discussion

This multiproxy-based study provides the first detailed examination of the interaction between local past sea ice variability (NØIB) and marine-terminating outlet glaciers and ice shelf evolution on the NEG continental shelf.

5.1. Late Weichselian Initial Deglaciation (>10 ka)

The retreat of ice across the continental shelf of NEG is recorded by mega-scale glacial lineations, grounding zone wedges, and moraines in both Norske Trough and Westwind Trough (Arndt et al., 2017; Evans et al., 2009; Winkelmann et al., 2010). Both 79NG and ZI had retreated to the present coast by 11.5–10.0 ka (Larsen et al., 2018.).

The lowest unit, LF1, in Core PS100/270 is characterized by a stiff, overconsolidated diamicton that we interpret as a subglacial till, which implies, that the location of Core PS100/270 on the inner continental shelf was covered by grounded ice as 79NG marine-terminating outlet glacier retreated from the continental shelf (Figure 3). Core PS2623 obtained from the south of Shannon Island on the East Greenland shelf also shows a lithostratigraphy that is similar to the one of Core PS100/270 (Figure 3), with overconsolidated diamict layers characterized by maximum values of IRD, magnetic susceptibility, and WDB during the initial deglaciation (Figure 3; Stein, 2008). A terrestrial source is supported by the dark reddish to gray sandy, silt matrix that constitutes the diamicton which points to a mid-Devonian sand/siltstones source originating from the NEG hinterland (Stein et al., 1996, 2016; Stein, 2008). In addition, this is supported by the lack of foraminifera within this unit (Figures 5, 8). The presence of biomarkers with relatively low HBIs and higher terrigenous and phytoplankton biomarkers values may indicate high amounts of reworked terrestrial material within the subglacial till that were transported during glacial retreat toward our core location (Figures 6 and 7). Based on this assumption no accumulation rates can be calculated for LF1. Given our present understanding of the deglacial history of the inner shelf and present coast of NEG this diamict was probably deposited between 13–10 ka as ice moved back onshore (Larsen et al., 2018). The age model derived for PS100/270 suggests the transition from the subglacial till to overlying laminated unit (hence an estimate of the timing of deglaciation at this core site) took place near 10.1 ka (Figure 2 and Table 2). With the grounded ice present, sea ice formation, open-water productivity and terrigenous input via sea ice melt was absent during this interval.

5.2. Early Holocene (~10 to 9.6 ka)

The overconsolidated subglacial till is overlain by a silty clay consisting of rhythmical irregular and indistinct laminations (Figure 3). This switch from LF1 to LF2 reflects a transition from subglacial conditions to proximal glaciomarine conditions as 79NG grounding-line retreated westward. Sedimentation rates in unit LF2 of Core PS100/270 are very high at this point reaching ~800–900 cm kyr^{-1} (Figure 2) and reflects an excess of sediment being pumped into suspension from the proximal glacial margin.

Further, the laminated nature of LF2 and high sedimentation rates indicate ice proximal conditions until at least 9.6 ka, suggesting that the grounded 79NG was relatively stable for at least a few hundred years. The intercalated diamicton horizons with increased clasts at 820 and 740 cm might be related to debris flows in a glaciomarine environment, phases of increased IRD supply possibly linked to iceberg calving from the proximal ice margin, or a readvance of the ice tongue of 79NG. Hence, the lower part of Core PS100/270 are dominated by sediments derived in a proximal proglacial environment. A similar situation is also recorded in the lithofacies of Core PS2623 where the alternations of diamictons and laminated sediments are interpreted as advance and retreat of the ice margin (Figure 3; Stein, 2008).

Highest sympagic, pelagic and terrigenous biomarker and bulk parameter concentrations and accumulation rates of Core PS100/270 mark the transition from subglacial to an open coastal environment with warmer conditions during the early Holocene Thermal Maximum (HTM) with peak solar insolation values (Figures 6 and 7; Laskar et al., 2004).

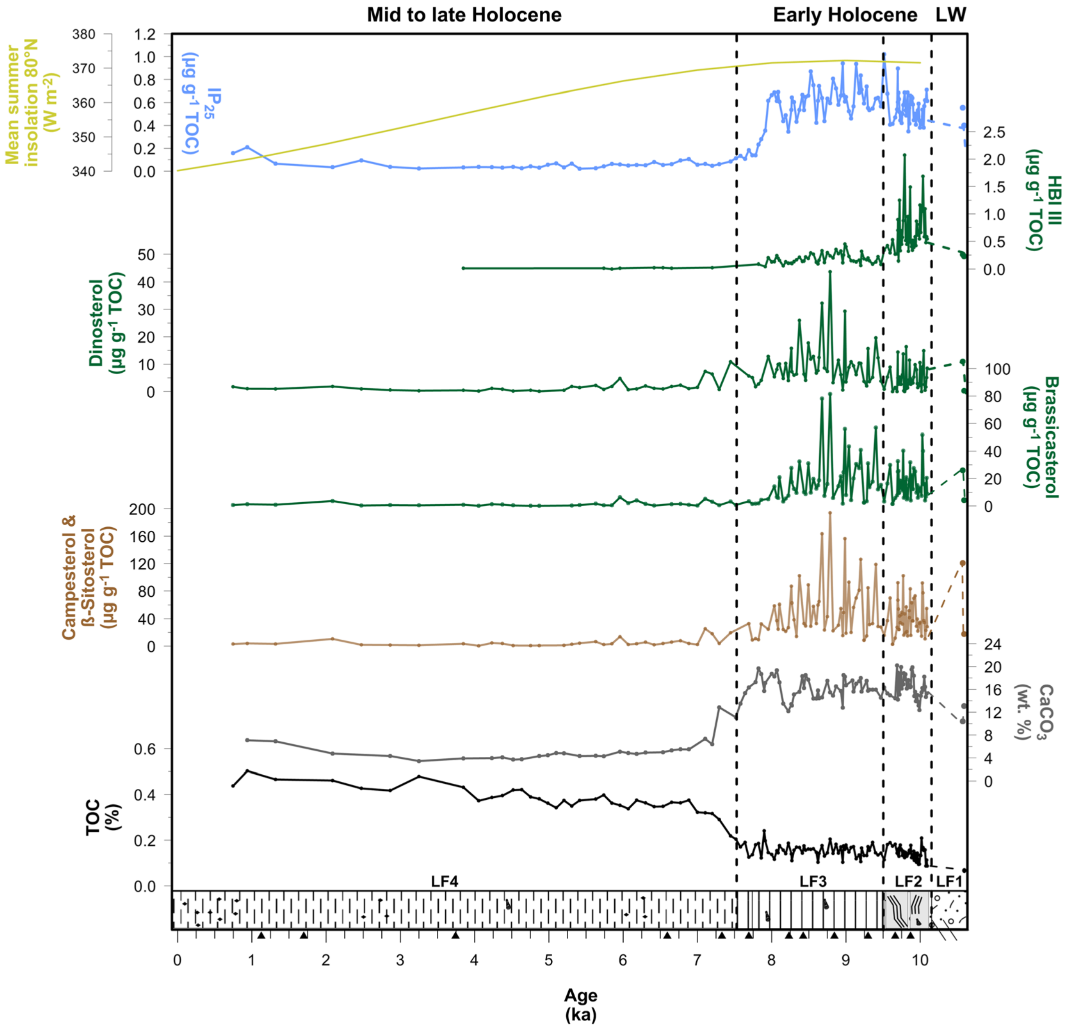

Figure 6. Lithology (divided into four lithofacies, LF1–4), total organic (TOC) and inorganic ($CaCO_3$) carbon (%), lipid biomarker concentrations (μg g^{-1} TOC) and mean summer solar insolation (W m^{-2}, Laskar et al., 2004), plotted against age (ka).

Rising air temperatures (~8°C warmer than preindustrial level, NEEM ice core record) and sea surface temperatures (2–5°C), may have forced an earlier nearly complete seasonal breakup of the local NØIB probably starting already in April/May (which is comparable to the present-day situation at the end of July) (Figure 1c; Andersen et al., 2004; Bauch et al., 2001; Bendle & Rosell-Melé, 2007; Buizert et al., 2018; Rimbu et al., 2003; Zehnich et al., 2020). This is evidenced by high IP_{25} concentrations and accumulation rates, suggesting increased sea ice breakup, thinning, and local drifting of NØIB ice floes. This enabled light and nutrients to penetrate through seasonal sea ice formation in spring/summer and favor sea ice algae (Figures 6 and 7). Sympagic producers of IP_{25} correlate positively with pelagic producers of HBI III, most likely indicating the predominance of well-developed MIZ conditions (Figures 6 and 7). Seasonal to marginal sea ice conditions are shown in the IP_{25} versus phytoplankton biomarkers brassicasterol and dinosterol relationship (Figure 9), consistent with PIP_{25} indices fluctuating around 0.6 (Figure 10). This environmental setting offers ideal conditions for production of all lipid biomarkers between 9.6 to ~10 ka on the inner NEG continental shelf (Figures 7 and 11). Additionally, high terrigenous biomarker concentration and accumulation rates show that sea ice melt released terrigenous particles and bound nutrients into the water column, triggering pelagic primary productivity as reflected in the increased phytoplankton biomarker fluxes (Figure 7). Highest $CaCO_3$ contents and accumulation rates are interpreted as increased supply of detrital carbonate (Figures 6 and 7), based on the negative correlation between carbonate and foraminifers

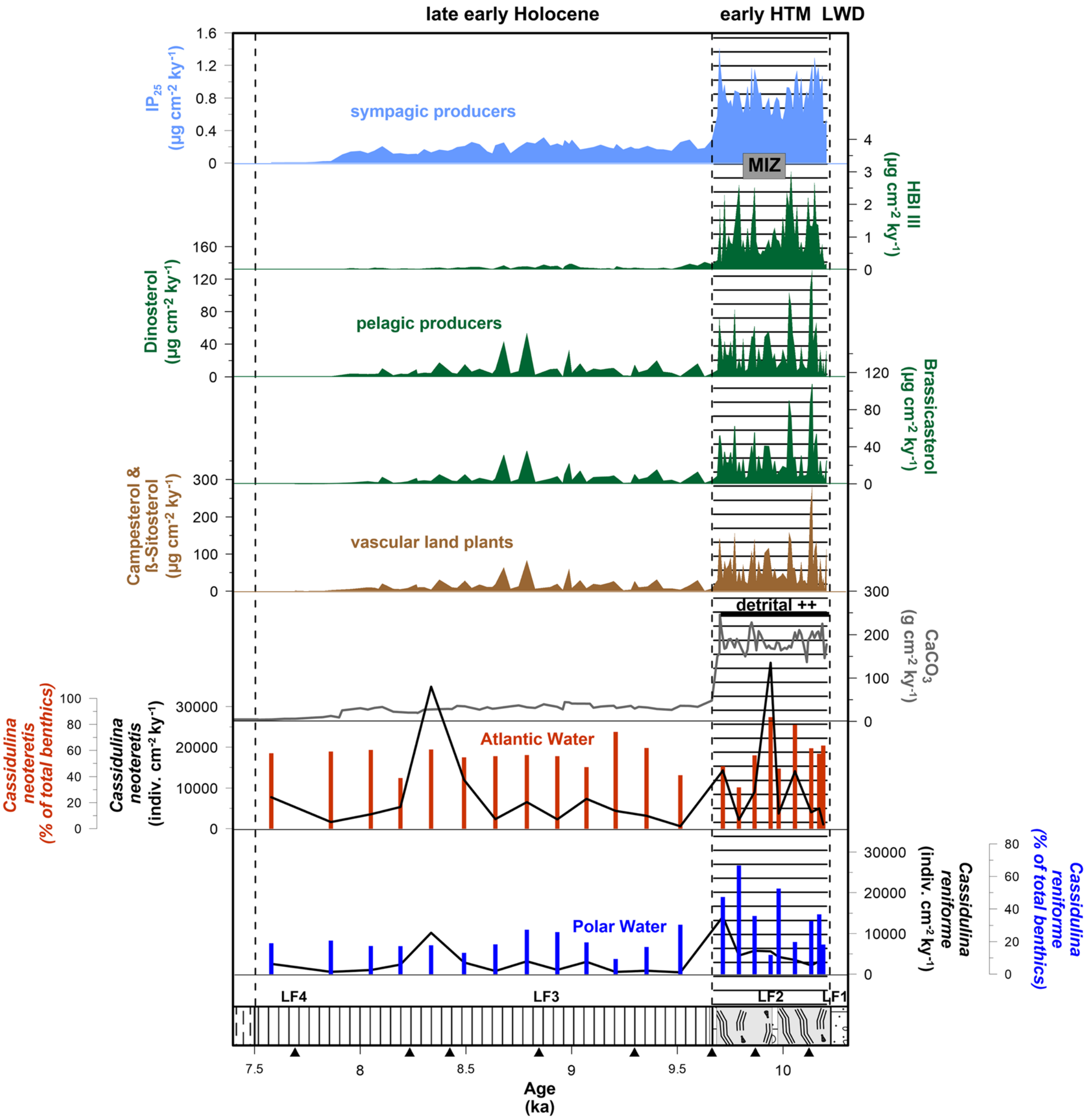

Figure 7. Accumulation rates (µg cm^{-2} kyr^{-1}, indiv. cm^{-2} kyr^{-1}) of total organic (TOC) and inorganic carbon (CaCO$_3$), terrigenous biomarkers (ß-sitosterol, campesterol), phytoplankton biomarkers (brassicasterol, dinosterol, HBI III), sea ice associated biomarker (IP$_{25}$), cold and warm water benthic foraminifera, plotted against age (ka). Foraminiferal relative abundance is shown by the bars and accumulation rates are shown by the solid lines. Hatched area marks highest concentrations of all markers in the marginal ice zone = MIZ.

(Figure S2). Furthermore, PIP$_{25}$ values show a very prominent short-term variability that might reflect short-term cyclic changes in sea ice extent (Figure 10). Such cyclicity was also found in Core PS93/025 (Figure 1) at the outer NEG continental shelf (Syring et al., 2020) and linked to cyclic changes in solar activity as a potential driving force (e.g., Vonmoos et al., 2006).

Meanwhile, rising air temperatures resulted in intensified surface melt of the GIS (MacGregor et al., 2016), while regional records show a strengthened West Spitsbergen Current at this time (Jennings et al., 2011), potentially increasing the flux of recirculating AW onto the NEG continental shelf within the Return Atlantic Current (RAC) (Bauch et al., 2001; Evans et al., 2009; Schaffer et al., 2020; Zehnich et al., 2020). Indeed, this is supported by the dominance of the benthic foraminifera, *Cassidulina neoteretis* (Figures 7 and 8), typically indicating presence of AW (e.g., Hald & Korsun, 1997), within the lower section of the laminated unit immediately after the transition from the subglacial till. This indicates a strong presence of

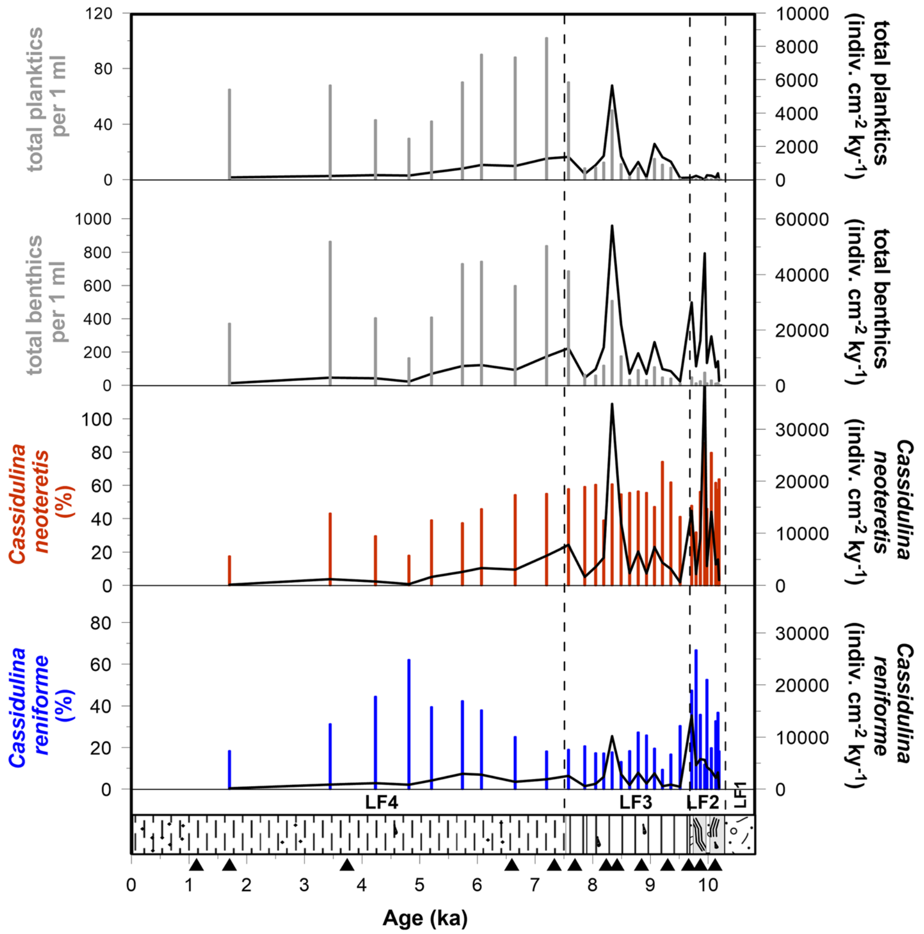

Figure 8. Relative abundance (bars) and accumulation rate (solid black lines) of *Cassidulina reniforme* (cold water indicator) and *Cassidulina neoteretis* (warm water indicator) plotted against age (ka). Absolute abundance (gray bars) and accumulation rates (solid black lines) of planktic and benthic foraminifera plotted against age (ka). The major lithofacies units LF1 to LF4 are shown to the left. Black triangles mark position of corrected ^{14}C AMS dates.

recirculating AW on the inner continental shelf of NEG immediately on deglaciation of the PS100/270 core site (Figure 11).

A strong westward advection of AW onto the NEG continental shelf at that time is also reflected in the assemblages and isotope data of planktic and benthic foraminifers determined at the nearby Core PS93/025 (Zehnich et al., 2020). The increased AW influence probably caused relatively high levels of basal melting at the grounding line or of any ice shelf present within Norske or Westwind Troughs.

The relatively high abundance of *Cassidulina reniforme* (a typical glaciomarine indicator) and presence (although only present in one sample) of *Stetsonia horvathi* support the interpretation of this transition indicating proximal glaciomarine conditions (Figures 5 and 8). It is likely that the mix of relatively cold and fresh meltwater from the grounded margin along with the presence of relatively warm and saline recirculating AW produces the mixed and variable assemblage within the lower laminated unit (Figure 8; Evans et al., 2009; Schaffer et al., 2020).

Highest accumulation rates of *Cassidulina neoteretis* and *Cassidulina reniforme* support these findings (Figure 8). A planktic foraminifera-based study by Hald et al. (2007) on six high-resolution sediment cores identifies variations in temperature and extent of AW in the northern North Atlantic during the Holocene, suggesting that there was a time-transgressive intensified warm AW inflow from south toward the Arctic Ocean during the late early Holocene. Werner et al. (2016) stated that the higher influx of warm AW was the result of large-scale reorganization of the ocean circulation during the Holocene.

In combination the sedimentological parameters, the presence of relatively warm water benthic foraminifers, sea ice associated biomarker IP_{25} consistent with high sterol concentrations and accumulation rates and the IP_{25}-phytoplankton biomarker relationship determined in Core PS100/270, all strongly support the existence of an extensive, but seasonal sea ice cover, and high overall productivity with pelagic spring/summer blooms and high terrigenous input (Figures 7, 8, and 9). Certainly, warmer atmospheric conditions and also the flux of relatively warm recirculating AW strongly controlled the onset of intensive thinning, mass ice loss, and grounding-line retreat inland during the HTM. Together with the disintegration of NØIB, it is assumed that the reduced buttressing effect on the ice shelf would have encouraged increased ice discharge due to the speed up of 79NG and ZI, facilitating rapid ice margin disintegration and glacier retreat. Results of Core PS100/270 correspond well to model simulations by Dyck et al. (2010) and other paleoclimate reconstructions from the outer NEG continental shelf (PS93/025) which infer a general decrease of sea ice concentrations during the early HTM, driven by the combination of an atmospheric and ocean forcing (Figure 11; Syring et al., 2020; Zehnich et al., 2020).

5.3. Late Early Holocene (9.6 to 7.5 ka)

Late early Holocene sediments are characterized by the deposition of finely laminated silty clays, and reflect a more distal proglacial environment as the grounded ice stream margin and ice shelf retreated inland (Figure 3). After 9.6 ka sedimentation rates on the inner shelf abruptly reduce from >800 cm kyr^{-1}, but still remain relatively high during this time (>200 cm kyr^{-1}, Figure 2). Only minor abundances of granule to gravel sized clasts (possibly IRD) were observed from core X-raydiographs and during sample investigations within our sedimentary facies, supporting suspension settling from 79NG meltwater plumes, that is, a predominance of meltwater-derived sedimentation (Figure 3). Furthermore, generally low concentration of IRD over the entire record, might indicate the influence of cold, fresh polar waters (linked to the EGC), preventing iceberg melt and release of ice rafted debris to the core site. The environmental conditions seem to be similar to those recorded at Core PS2623 were also minimum IRD was found in this interval (Figure 3; Stein, 2008).

Lipid biomarker concentrations are similar to early HTM values, while absolute accumulations rates are 2 to 3 times lower during this interval. Also notable, however, is the abrupt decrease of the open-water phytoplankton biomarker HBI III (Figures 6 and 7). Based on our records, we therefore assume a change in environmental conditions from a stable sea ice margin toward the formation of a more extensive seasonal (spring) landfast sea ice cover (NØIB), comparable to satellite images from modern times (Figure 1c, beginning of May). Knowledge about modern conditions are based on instrumental data/measurements (e.g., satellite-derived images) rather than our proxy data.

The occurrence of a strong pycnocline might have separated the surface from the subsurface water layer during this interval. Meltwater/Freshwater from the surrounding glaciers formed a cold, low salinity sea ice fed surface layer, but lowered sea ice algae growth due to the lack of brine formation through salt ions at the underside of the sea ice (Belt, 2018; Limoges et al., 2018; Werner et al., 2016). Underneath lies the warm Atlantic subsurface layer, and below that flows the cold, fresh polar water from the Arctic Ocean. Both would explain the continued presence of warm and cold foraminifera species (Werner et al., 2016).

At the same time, HBI III concentrations are extremely low throughout the interval of elevated IP_{25} concentrations during the late early Holocene, suggesting an extensive sea ice cover associated with harsh winters and only short (nearly ice-free) summers on the inner NEG continental shelf (Figures 6 and 7). Summers with shorter periods of open-water areas, increased algae productivity and sea ice melt would explain the lower accumulation rates of the phytoplankton markers brassicasterol and dinosterol, as well as lower accumulation rates of terrigenous biomarkers campesterol and ß-sitosterol (Figures 6 and 7). Our interpretation of extended sea ice conditions at this time is illustrated in the IP_{25}/phytoplankton biomarker plot (Figure 9).

During this interval the benthic foraminiferal assemblage (Figure 5) as well as their high accumulation rates (Figures 7 and 8) indicate a strong influence of recirculating AW within the RAC recorded at Core PS100/270. This is supported by the dominance of *C. neoteretis* (60%), with low relative abundance of *C. reniforme* through the record and also other relatively warm water indicators also increasing (e.g., *Nonionella iridea* and *Melonis barleeanum*) (Figure 8). However, the presence of *Stetsonia horvathi* and *Glomulina oculus* through this interval also supports the interpretation of more extensive sea ice during this interval (both

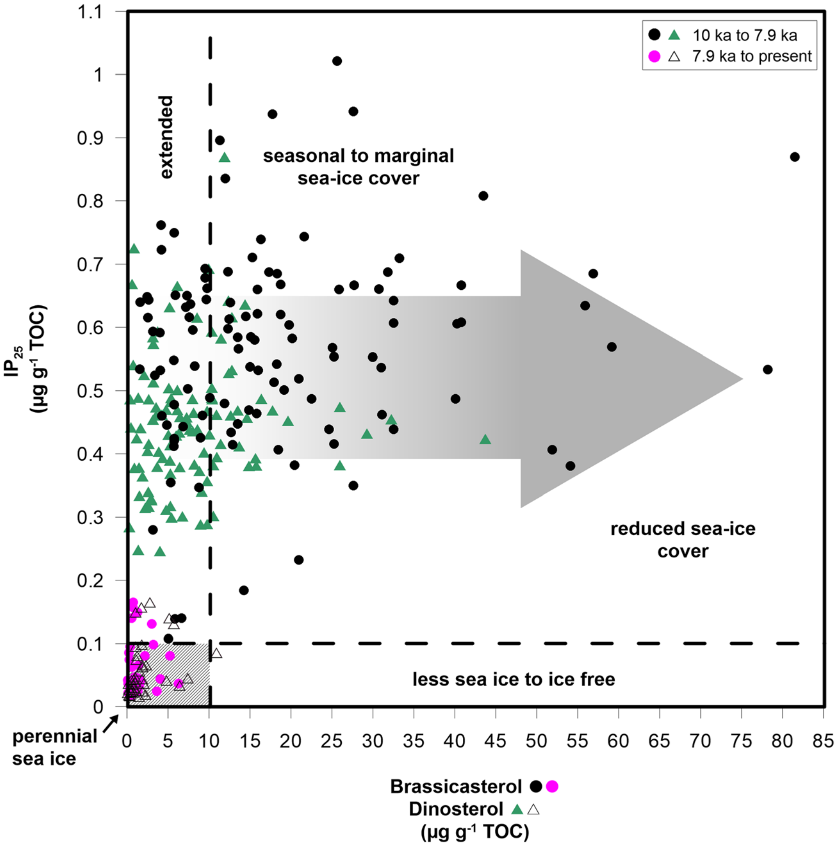

Figure 9. Sea ice associated biomarker IP_{25} (μg g^{-1} TOC) versus phytoplankton biomarkers brassicasterol and dinosterol (μg g^{-1} TOC). Black dot and green triangle show phytoplankton marker concentrations from the interval between 10 to 7.5 ka and pink dot and white triangle from the interval between 7.5 to present. Classification of different sea ice settings are according to Müller et al. (2011). Large gray arrow indicates transition from most extended sea ice conditions to reduced sea ice cover. Most of the data points between 7.5 ka to present occur in the lower left corner, representing extended to perennial sea ice conditions.

species commonly found in regions influenced by a high concentration of sea ice, for example, Jennings et al., 2020; Wollenburg & Mackensen, 1998). Continuing high but variable AW advection toward the NEG continental shelf until about 8 ka is also recorded in the assemblages and isotope data of foraminifers at Core PS93/25 (Zehnich et al., 2020) as well as Core PS1230 (Bauch et al., 2001). This would potentially encourage relatively high rates of basal melting of the floating ice tongue of 79NG glacier and at the grounding line. This basal meltwater rises up, leading to a stratification of the water column with the cold, fresh and relatively low-density meltwater layer spreading underneath the fast ice separating it from the warmer, more salty and denser sea water below. Thus, the colder water layer acts as a barrier and additionally stabilizes the fast ice (Mayer et al., 2000). In addition, the supply of freshwater to the NEG continental shelf may trigger changes in the local fjord, marine productivity, ocean and atmospheric temperatures (Bamber et al., 2012; Cape et al., 2019; Straneo & Cenedese, 2015).

The extensive seasonal sea ice conditions (development of NØIB) and the further retreat of 79NG due to basal melting and grounding-line retreat recorded at core site PS100/270 are highlighted in Figure 11. This fits with previous investigations from 79NG fjord that suggest ice shelf disintegration between 9.0–7.7 ka (Bennike & Weideck, 2001). These interpretations are consistent with modern observations and support the suggestion that the recent enhanced intrusion of warm recirculating AW (e.g., warmer waters between 0.5–0.8°C in 2006–2007) and rising atmospheric temperatures make both 79NG and ZI particularly vulnerable to surface and submarine melting (Beszczynska-Möller et al., 2012; Holland et al., 2008; Ingleby & Huddleston, 2007; Schaffer et al., 2020; Seale et al., 2011).

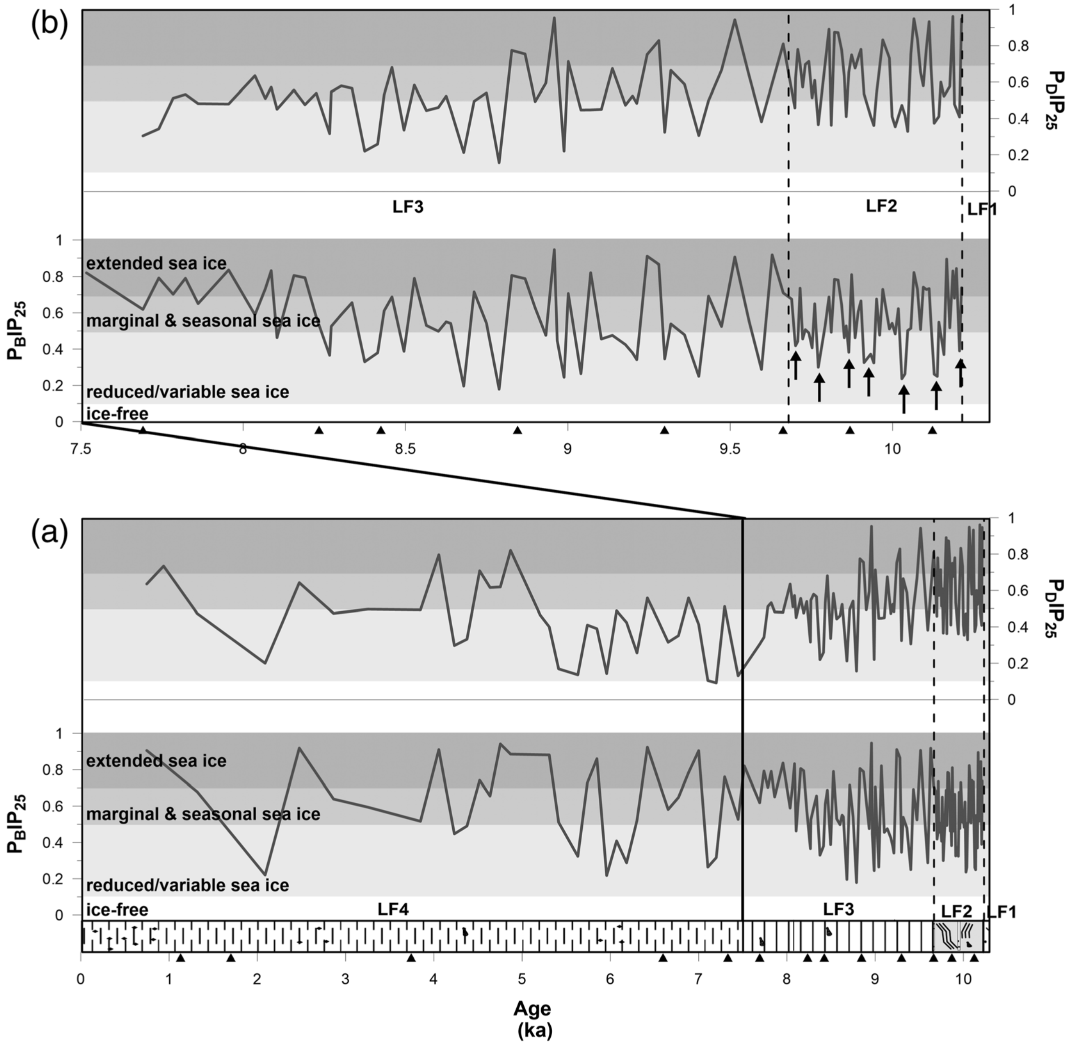

Figure 10. P_BIP_{25} and P_DIP_{25} indices of GC PS100/270, plotted against age (ka). (a) Complete Holocene record, (b) the early Holocene. PIP_{25} values <0.1 indicate ice-free conditions, between 0.1 to 0.5 a reduced/variable sea ice cover, between 0.5 to 0.8 seasonal to marginal sea ice conditions and above 0.8 extended to perennial sea ice cover (classification according to Müller et al., 2011). Black triangles mark the corrected ^{14}C-dated AMS core depths. Black arrows indicate short-term cyclic variations within the record.

5.4. Middle to Late Holocene (7.5 to ~0.7 ka)

After the total ice shelf break up and grounding-line retreat of 79NG toward the inner fjord at ~7.5 ka (Figure 11), the sedimentary regime at core site PS100/270 was dominated by a hemipelagic massive brownish silty clay to clay with sedimentation rates decrease significantly (Figure 3) indicating a change to a distal glaciomarine environment.

The decrease of all biomarker concentrations and accumulation rates to minimum values confirm the presence of a lasting to nearly permanent sea ice cover (NØIB) with extremely low primary productivity during the mid to late Holocene (Figures 6 and 7). During the summer months, biomarker records indicate only sufficient thinning of the sea ice cover to allow very minor productivity of brassicasterol, dinosterol, and HBI III (Figure 7).

However, preservation of organic matter is often susceptible to diagenetic alteration (chemical, physical, or biological processes) in the water column or sediment and therefore concentrations can be underestimated

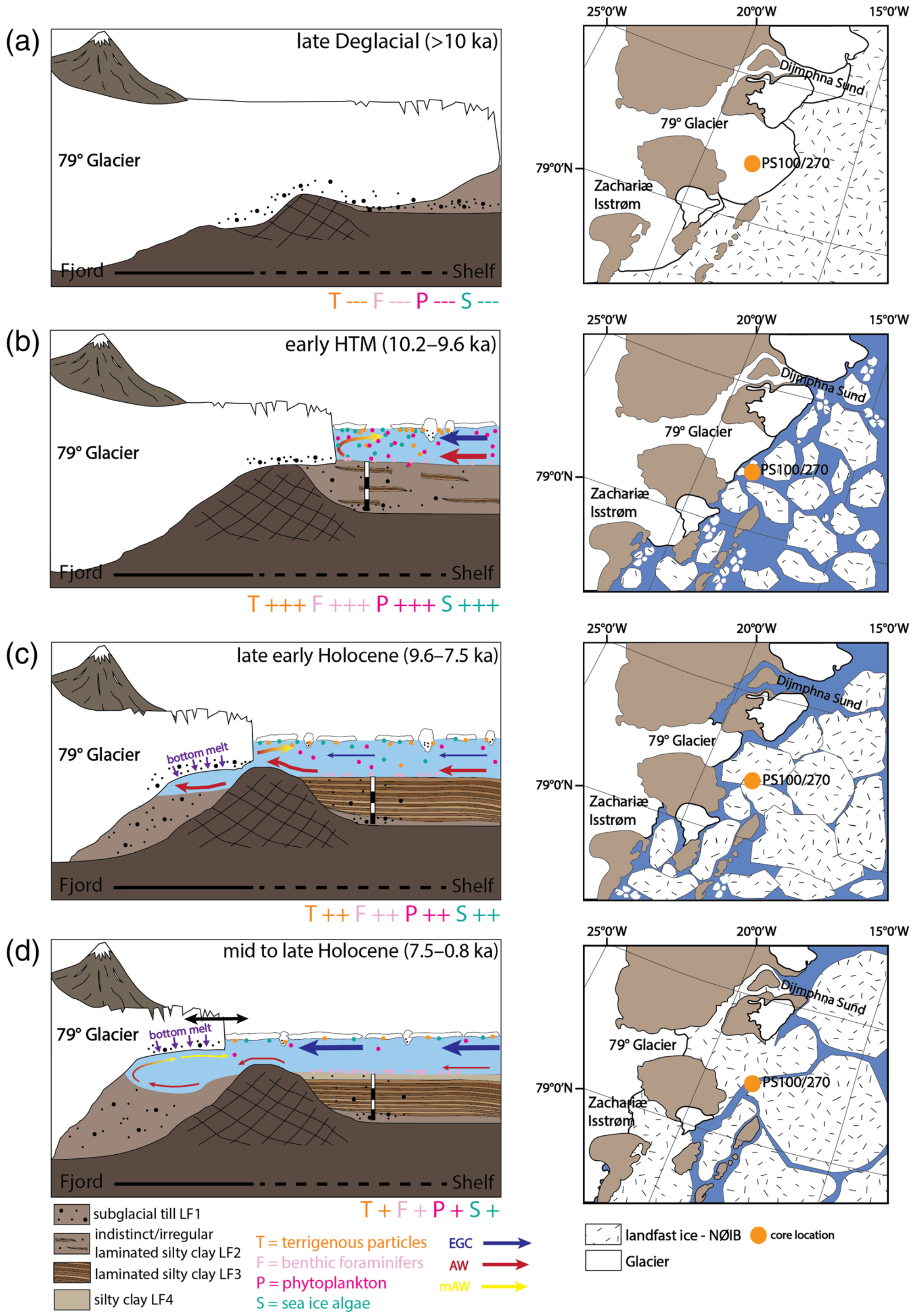

Figure 11. Conceptual model representing the interaction between local sea ice formation, 79NG retreat and ocean circulation on the NEG continental shelf. The four stages (a) to (d) represent the time intervals of lithofacies units LF1–4: (a) the initial late Weichselian deglacial (>10 ka), (b) early Holocene thermal maximum (10.2–9.6 ka), (c) late early Holocene (9.6–7.5 ka), and (d) middle to late Holocene (7.5–0.7 ka) (according to Schaffer et al., 2020). The black and white bar represents the core location. The thicknesses of colored arrows indicate stronger/weaker influence of East Greenland current = EGC (blue), warm recirculating Atlantic water = AW (red) and modified recirculating Atlantic water = mAW (yellow). Top views of the research area to the right show 79NG retreat and extension of the Norske Øer ice barrier (NØIB) during these four stages.

(Leventer, 2013; Rontani et al., 2014, 2018). We cannot exclude the possibility that the signal was partially altered, especially looking at the sterols that show a very similar trend.

The IP_{25} versus phytoplankton biomarkers brassicasterol and dinosterol relationship (Figure 9) points to a predominantly perennial sea ice cover during the middleqw to late Holocene, PIP_{25} indices demonstrate stable seasonal sea ice conditions, with occasional intervals of extended to perennial sea ice conditions (Figure 11). Sneed and Hamilton (2016) described the modern NØIB as a region of perennial landfast ice, varying annually in thickness and extent, but also more frequent seasonal breakup since 2007.

The relative abundance of *C. neoteretis* remains relatively high until approx. 6.5 ka, but then starts to fall as the relatively cold water indicator, *C. reniforme*, increases to over 40% of the assemblage from 6 to 2.5 ka (Figure 8). Although relative abundances of foraminifera are high during this interval (Figure 5), accumulation rates of both benthic species (cold and warm) clearly indicate a decreasing trend (Figure 8). This may suggest a continued presence of relatively warm recirculating AW through the middle to late Holocene, but potentially a reduction in flux of this warmer water to the inner continental shelf. The dominance of *C. reniforme* supports this along with a slight increase in abundance of *S. horvathi*, an indicator of harsh conditions, often found below perennial sea ice or an ice shelf. This would most likely reduce the basal melting driven by ocean circulation along the inner continental shelf and within the 79NG fjord and may have contributed to the readvance of the ice shelf through the 79NG fjord from around ~4.5 ka onward (Bennike & Weideck, 2001) (Figure 11). A cooler subsurface recirculating AW on the NEG shelf also correlates well with a cooling in Atlantic sourced waters recorded in the Fram Strait since 6 ka (Werner et al., 2016). This relative cooling in subsurface water conditions corresponds well with the Neoglacial Cooling trend linked with decreasing solar insolation, a southward shift of the polar front and a slowdown of the supply of warm Atlantic Water masses identified in many regions of Greenland (e.g., Jennings et al., 2002; Koç et al., 1993; McGregor et al., 2015; McKay et al., 2018).

In fact, minimum solar insolation and a strengthened EGC, evidenced by lowered SST, support the influence of colder polar waters toward the inner shelf during the middle to late Holocene (Bauch et al., 2001; Jennings et al., 2002; Laskar et al., 2004; Müller et al., 2012; Ran et al., 2006). The overall onset of harsh conditions with relatively low biomarker concentrations and cooler SST were also observed at the outer NEG core site PS93/025 and at the inner East Greenland margin (PS2641) (Kolling et al., 2017; Syring et al., 2020, Zehnich et al., 2020).

Sedimentation rate reduces significantly in the upper section of the core leading to lower temporal resolution in our record, hence, identification of shorter term variability is not possible from this record.

6. Conclusion

Detailed sedimentological, organic geochemical and foraminiferal investigations of Core PS100/270 from the inner NEG shelf reflect distinct changes in 79NG and sea ice conditions during the end of the last glacial period and through the Holocene. Nevertheless, the last ~1 ka could not be resolved in our records. The 79NG retreated from the core site at ~10.2 ka and stayed close until 9.6 ka indicated by highest sedimentation rates in a proximal glaciomarine environment. The grounding line of 79NG may have been pinned at the islands at the mouth of the fjord at this time, but between 9.6 and 7.5 ka, both the grounding line and ice shelf had retreated through the fjord, and this is reflected by a significantly decreasing sedimentation rate.

The records presented here, show a rapid 79NG retreat and ice shelf disintegration during the early Holocene between 9.6 to 7.5 ka, while sea ice formation increased during the Holocene. Terrigenous matter supply and/or surface productivity are mainly influenced by fluctuations in the Greenland ice sheet dynamics, meltwater input, iceberg drift, seasonal buildup of NØIB, and ocean circulation. Rising air temperatures and the influence of warm AW advection are assumed to be the main drivers. Overall four different stages of 79NG retreat and increased sea ice formation have been identified during the end of the late Weichselian deglaciation into the Holocene:

1. Late Weichselian deglacial conditions with a grounded 79NG covering the core location PS100/270, indicated by deposition of a subglacial till.
2. Onset of rapid 79NG retreat during the early HTM due to increased inflow of warm recirculating AW toward the inner NEG shelf, proximal glaciomarine sedimentation off a grounded ice margin pinned

on the inner NEG shelf, predominance of seasonal to marginal sea ice conditions characterized by short-term cyclic variability probably linked to cyclic changes in solar activity, and overall high marine productivity and input of terrigenous matter during the early HTM.

3. Retreat of 79NG from 9.6 to 7.5 ka toward the inner fjord and continuing high AW advection, increased prolonged seasonal sea ice conditions, lowered primary productivity, and periods of sea ice melting during shorter summers occurring in the late early Holocene.
4. Harsher conditions during the middle to late Holocene with a weaker warm recirculating AW advection and a more extensive seasonal sea ice cover (development of NIØB) with a nearly absent primary production.

Data Availability Statement

All data, including downcore biomarker and bulk parameter concentrations ($\mu g\ g^{-1}$ TOC, $\mu g\ g^{-1}$ Sed), as well as accumulation rates ($\mu g\ cm^{-2}\ kyr^{-1}$, $g\ cm^{-2}\ kyr^{-1}$), foraminifers' assemblages (total benthics and planktics per 1 ml) and calibrated ages (ka) are available from Pangaea (doi: https://doi.org/10.1594/PANGAEA.921185).

Acknowledgments

We gratefully thank Captains Schwarze and Wunderlich and the of RV *Polarstern* as well Chief Scientist Torsten Kanzow (PS100 + PS109) for excellent support and cooperation during both cruises. Thanks to Walter Luttmer/AWI for technical support during the laboratory work, and Gesine Mollenhauer/AWI for high-precision express analyses of small-scale ^{14}C samples with the AWI MICADAS system. Thanks to Simon Belt (Biogeochemistry Research Centre, University of Plymouth/UK) for providing the 7-HND standard for IP_{25} quantification. ASI-AMSR2 sea ice concentration data were provided from this site (https://seaice.uni-bremen.de/). This publication is a contribution to the Research Program PACES II, Topic 3 (The earth system from a polar perspective: Data, modeling, and synthesis) of the Alfred Wegener Institute Helmholtz Centre for Polar und Marine Research (AWI). The studied samples and data were provided by AWI (Grant AWI-PS100). This research was also supported by the UK NERC (Grant NE/N011228/1) and NERC Radiocarbon Laboratory Grant 2113.0418. Open access funding enabled and organized by Projekt DEAL.

References

Abdalati, W., & Steffen, K. (2001). Greenland Ice Sheet melt extent: 1979–1999. *Journal of Geophysical Research*, *106*(D24), 33,983–33,988. https://doi.org/10.1029/2001JD900181

Andersen, C., Koç, N., Jennings, A., & Andrews, J. T. (2004). Nonuniform response of the major surface currents in the Nordic Seas to insolation forcing: Implications for the Holocene climate variability. *Paleoceanography*, *19*, PA2003. https://doi.org/10.1029/2002PA000873

Arndt, J. E., Jokat, W., & Dorschel, B. (2017). The last glaciation and deglaciation of the Northeast Greenland continental shelf revealed by hydro-acoustic data. *Quaternary Science Reviews*, *160*, 45–56. https://doi.org/10.1016/j.quascirev.2017.01.018

Arndt, J. E., Jokat, W., Myklebust, J. A., Dowdeswell, A., & Evans, J. (2015). A new bathymetry of the Northeast Greenland continental shelf: Constraints on glacial and other processes. *Geochemistry, Geophysics, Geosystems*, *16*, 3733–3753. https://doi.org/10.1002/2015GC005931

Bamber, J., van den Broeke, M., Ettema, J., Lenaerts, J., & Rignot, E. (2012). Recent large increases in freshwater fluxes from Greenland into the North Atlantic. *Geophysical Research Letters*, *39*, L19501. https://doi.org/10.1029/2012GL052552

Bauch, H. A., Erlenkeuser, H., Spielhagen, R. F., Struck, U., Matthiessen, J., Thiede, J., & Heinemeier, J. (2001). A multiproxy reconstruction of the evolution of deep and surface waters in the subarctic Nordic seas over the last 30,000yr. *Quaternary Science Reviews*, *20*(4), 659–678. https://doi.org/10.1016/S0277-3791(00)00098-6

Belt, S. T. (2018). Organic geochemistry source-specific biomarkers as proxies for Arctic and Antarctic sea ice. *Organic Geochemistry*, *125*, 277–298. https://doi.org/10.1016/j.orggeochem.2018.10.002

Belt, S. T. (2019). What do IP_{25} and related biomarkers really reveal about sea ice change? *Quaternary Science Reviews*, *204*, 216–219. https://doi.org/10.1016/j.quascirev.2018.11.025

Belt, S. T., Brown, T. A., Smik, L., Tatarek, A., Wiktor, J., Stowasser, G., et al. (2017). Identification of C_{25} highly branched isoprenoid (HBI) alkenes in diatoms of the genus *Rhizosolenia* in polar and sub-polar marine phytoplankton. *Organic Geochemistry*, *110*, 65–72. https://doi.org/10.1016/j.orggeochem.2017.05.007

Belt, S. T., Cabedo-Sanz, P., Smik, L., Navarro-Rodriguez, A., Berben, S. M. P., Knies, J., & Husum, K. (2015). Identification of paleo Arctic winter sea ice limits and the marginal ice zone: Optimised biomarker-based reconstructions of late Quaternary Arctic sea ice. *Earth and Planetary Science Letters*, *431*, 127–139. https://doi.org/10.1016/j.epsl.2015.09.020

Belt, S. T., Massé, G., Rowland, S. J., Poulin, M., Michel, C., & LeBlanc, B. (2007). A novel chemical fossil of palaeo sea ice: IP_{25}. *Organic Geochemistry*, *38*(1), 16–27. https://doi.org/10.1016/j.orggeochem.2006.09.013

Belt, S. T., & Müller, J. (2013). The Arctic sea ice biomarker IP_{25}: A review of current understanding, recommendations for future research and applications in palaeo sea ice reconstructions. *Quaternary Science Reviews*, *79*, 9–25. https://doi.org/10.1016/j.quascirev.2012.12.001

Belt, S. T., Smik, L., Brown, T. A., Kim, J.-H., Rowland, S. J., Allen, C. S., et al. (2016). Source identification and distribution reveals the potential of the geochemical Antarctic sea ice proxy $IPSO_{25}$. *Nature Communications*, *7*(1), 12655. https://doi.org/10.1038/ncomms12655

Bendle, J. A. P., & Rosell-Melé, A. (2007). High-resolution alkenone sea surface temperature variability on the North Icelandic Shelf: Implications for Nordic Seas palaeoclimatic development during the Holocene. *The Holocene*, *17*(1), 9–24. https://doi.org/10.1177/0959683607073269

Bennike, O., & Weideck, A. (2001). Late Quaternary history around Nioghalvfjerdsfjorden and Jøkelbugten, north-East Greenland. *Boreas*, *30*(3), 205–227. https://doi.org/10.1111/j.1502-3885.2001.tb01223.x

Beszczynska-Möller, A., Fahrbach, E., Schauer, U., & Hansen, E. (2012). Variability in Atlantic water temperature and transport at the entrance to the Arctic Ocean, 1997–2010. *ICES Journal of Marine Science*, *69*(5), 852–863. https://doi.org/10.1093/icesjms/fss05

Blaauw, M., & Christen, J. A. (2011). Flexible paleoclimate age-depth models using an autoregressive gamma process. *Bayesian Analysis*, *6*(3), 457–474. https://doi.org/10.1214/11-BA618

Boon, J. J., Rijpstra, W. C., De Lange, F., De Leeuw, J. W., Yoshioka, M., & Shimizu, Y. (1979). Black Sea sterol—A molecular fossil for dinoflagellate blooms. *Nature*, *277*(5692), 125–127. https://doi.org/10.1038/277125a

Bourke, R. H., & Garrett, R. P. (1987). Sea ice thickness distribution in the Arctic Ocean. *Cold Regions Science and Technology*, *13*(3), 259–280. https://doi.org/10.1016/0165-232X(87)90007-3

Brown, T. A., & Belt, S. T. (2016). Novel tri- and tetra-unsaturated highly branched isoprenoid (HBI) alkenes from the marine diatom Pleurosigma intermedium. *Organic Geochemistry*, *91*, 120–122. https://doi.org/10.1016/j.orggeochem.2015.11.008

Brown, T. A., Belt, S. T., Tatarek, A., & Mundy, C. J. (2014). Source identification of the Arctic sea ice proxy IP_{25}. *Nature Communications*, *5*(1), 1, 4197–7. https://doi.org/10.1038/ncomms5197

Budéus, G., & Schneider, W. (1995). On the hydrography of the Northeast Water Polynya. *Journal of Geophysical Research*, *100*(C3), 4287–4299. https://doi.org/10.1029/94JC02024

Budéus, G., Schneider, W., & Kattner, G. (1997). Distribution and exchange of water masses in the Northeast Water polynya (Greenland Sea). *Journal of Marine Systems*, *10*(1-4), 123–138. https://doi.org/10.1016/S0924-7963(96)00074-7

Buizert, C., Keisling, B. A., Box, J. E., He, F., Carlson, A. E., Sinclair, G., & DeConto, R. M. (2018). Greenland-wide seasonal temperatures during the Last Deglaciation. *Geophysical Research Letters*, *45*, 1905–1914. https://doi.org/10.1002/2017GL075601

Cape, M. R., Straneo, F., Beaird, N., Bundy, R. M., & Charette, M. A. (2019). Nutrient release to oceans from buoyancy-driven upwelling at Greenland tidewater glaciers. *Nature Geoscience*, *12*(1), 34–39. https://doi.org/10.1038/s41561-018-0268-4

Choi, Y., Morlighem, M., Rignot, E., Mouginot, J., & Wood, M. (2017). Modeling the response of Nioghalvfjerdsfjorden and Zachariae Isstrøm glaciers, Greenland, to ocean forcing over the next century. *Geophysical Research Letters*, *44*, 11,071–11,079. https://doi.org/10.1002/2017GL075174

Comiso, J. C., Parkinson, C. L., Gersten, R., & Stock, L. (2008). Accelerated decline in the Arctic sea ice cover. *Geophysical Research Letters*, *35*, L01703. https://doi.org/10.1029/2007GL031972

Dai, A., Luo, D., Song, M., & Liu, J. (2019). Arctic amplification is caused by sea-ice loss under increasing CO_2. *Nature Communications*, *10*(1), 121. https://doi.org/10.1038/s41467-018-07954-9

Day, J. J., Hargreaves, J. C., Annan, J. D., & Abe-Ouchi, A. (2012). Sources of multi-decadal variability in Arctic sea ice extent. *Environmental Research Letters*, *7*(3), 34011. https://doi.org/10.1088/1748-9326/7/3/034011

Dupont, T. K., & Alley, R. B. (2005). Assessment of the importance of ice-shelf buttressing to ice-sheet flow. *Geophysical Research Letters*, *32*, L04503. https://doi.org/10.1029/2004GL022024

Dyck, S., Tremblay, L. B., & de Vernal, A. (2010). Arctic Sea-ice cover from the early Holocene: The role of atmospheric circulation patterns. *Quaternary Science Reviews*, *29*(25-26), 3457–3467. https://doi.org/10.1016/j.quascirev.2010.05.008

Ehrmann, W. U., & Thiede, J. (1985). History of Mesozoic and Cenozoic sediment fluxes to the North Atlantic Ocean. *Contributions to Sedimentary Geology*, *15*.

Enderlin, E. M., Howat, I. M., Jeong, S., Noh, M.-J., van Angelen, J. H., & van den Broeke, M. R. (2014). An improved mass budget for the Greenland ice sheet. *Geophysical Research Letters*, *41*, 866–872. https://doi.org/10.1002/2013GL059010

Evans, J., Cofaigh, Ó., Dowdeswell, J. A., & Wadhams, P. (2009). Marine geophysical evidence for former expansion and flow of the Greenland Ice Sheet across the north-east Greenland continental shelf. *Journal of Quaternary Science*, *24*(3), 279–293. https://doi.org/10.1002/jqs.1231

Evans, J., Dowdeswell, J. A., Grobe, H., Niessen, F., Stein, R., Hubberten, H.-W., & Whittington, R. J. (2002). Late Quaternary sedimentation in Kejser Franz Joseph Fjord and the continental margin of East Greenland. *Special Publication. Geological Society of London*, *203*(1), 149–179. https://doi.org/10.1144/GSL.SP.2002.203.01.09

Fahl, K., & Stein, R. (2007). Biomarker records, organic carbon accumulation, and river discharge in the Holocene southern Kara Sea (Arctic Ocean). *Geo-Marine Letters*, *27*(1), 13–25. https://doi.org/10.1007/s00367-006-0049-8

Fahl, K., & Stein, R. (2012). Modern seasonal variability and deglacial/Holocene change of Central Arctic Ocean sea-ice cover: New insights from biomarker proxy records. *Earth and Planetary Science Letters*, *351-352*, 123–133. https://doi.org/10.1016/j.epsl.2012.07.009

Fahl, K., Stein, R., Gaye-Haake, B., Gebhardt, C., Kodina, L.A., Unger, D., & Ittekkot, V. (2003). Biomarkers in surface sediments from the Ob and Yenisei estuaries and southern Kara Sea: Evidence for particulate organic carbon sources, pathways, and degradation. In: Stein, R., Fahl, K., Fütterer, D.K., Galimov, E.M., Stepanets, O.V. (Eds.), Siberian.

Fahnestock, M., Bindschadler, R., Kwok, R., & Jezek, K. (1993). Greenland ice sheet surface properties and ice dynamics from ERS-1 SAR imagery. *Science*, *262*, 1530–1534. https://doi.org/10.1126/science.262.5139.1530

Hald, M., Andersson, C., Ebbesen, H., Jansen, E., Klitgaard-Kristensen, D., Risebrobakken, B., et al. (2007). Variations in temperature and extent of Atlantic water in the northern North Atlantic during the Holocene. *Quaternary Science Reviews*, *26*(25-28), 3423–3440. https://doi.org/10.1016/j.quascirev.2007.10.005

Hald, M., & Korsun, S. (1997). Distribution of modern benthic foraminifera from fjords of Svalbard, European Arctic. *Journal of Foraminiferal Research*, *27*(2), 101–122. https://doi.org/10.2113/gsjfr.27.2.101

Helm, V., Humbert, A., & Miller, H. (2014). Elevation and elevation change of Greenland and Antarctica derived from CryoSat-2. *The Cryosphere*, *8*, 1539–1559.

Higgins, A. K. (1989). North Greenland ice islands. *Polar Record (Gr. Brit)*, *25*(154), 207–212. https://doi.org/10.1017/S0032247400010809

Higgins, K. (1991). North Greenland glacier velocities and calf ice production. *Polarforschung*, *60*, 1–23.

Holland, D. M., Thomas, R. H., de Young, B., Ribergaard, M. H., & Lyberth, B. (2008). Acceleration of Jakobshavn Isbræ triggered by warm subsurface ocean waters. *Nature Geoscience*, *1*(10), 659–664. https://doi.org/10.1038/ngeo316

Hughes, N. E., Wilkinson, J. P., & Wadhams, P. (2011). Multi-satellite sensor analysis of fast-ice development in the Norske Øer ice barrier, Northeast Greenland. *Annals of Glaciology*, *52*(57), 151–160. https://doi.org/10.3189/172756411795931633

Ingleby, B., & Huddleston, M. (2007). Quality control of ocean temperature and salinity profiles — Historical and real-time data. *Journal of Marine Systems*, *65*(1-4), 158–175. https://doi.org/10.1016/j.jmarsys.2005.11.019

Jaffé, R., Wolff, G. A., Cabrera, A., & Carvajal Chitty, H. (1995). The biogeochemistry of lipids in rivers of the Orinoco Basin. *Geochimica et Cosmochimica Acta*, *59*(21), 4507–4522. https://doi.org/10.1016/0016-7037(95)00246-V

Jennings, A., Andrews, J., Reilly, B., Walczak, M., Jakobsson, M., Mix, A., et al. (2020). Modern foraminiferal assemblages in northern Nares Strait, Petermann Fjord, and beneath Petermann ice tongue, NW Greenland. *Arctic, Antarctic, and Alpine Research*, *52*(1), 491–511. https://doi.org/10.1080/15230430.2020.1806986

Jennings, A., Andrews, J., & Wilson, L. (2011). Holocene environmental evolution of the SE Greenland shelf north and south of the Denmark Strait: Irminger and East Greenland current interactions. *Quaternary Science Reviews*, *30*(7-8), 980–998. https://doi.org/10.1016/j.quascirev.2011.01.016

Jennings, A. E., Knudsen, K. L., Hald, M., Hansen, C. V., & Andrews, J. T. (2002). A mid-Holocene shift in Arctic Sea-ice variability on the East Greenland shelf. *The Holocene*, *12*(1), 49–58. https://doi.org/10.1191/0959683602hl519rp

Johnson, M., & Niebauer, H. J. (1995). The 1992 summer circulation in the northeast water Polynya from acoustic Doppler current profiler measurements. *Journal of Geophysical Research*, *100*(C3), 4301–4307. https://doi.org/10.1029/94JC01981

Joughin, I., Fahnestock, M., MacAyeal, D., Bamber, J. L., & Gogineni, P. (2001). Observation and analysis of ice flow in the largest Greenland ice stream. *Journal of Geophysical Research*, *106*(D24), 34,021–34,034. https://doi.org/10.1029/2001JD900087

Kanzow, T. (2017). The expedition PS100 of the research vessel POLARSTERN to the Greenland Sea and the Fram Strait in 2016. Reports on Polar and Marine Research, Alfred Wegener Institute for Polar and Marine Research, Bremerhaven, No. 705.

Kaufman, D. S., Ager, T. A., Anderson, N. J., Anderson, P. M., Andrews, J. T., Bartlein, P. J., et al. (2004). Holocene thermal maximum in the western Arctic (0-180 W). *Quaternary Science Reviews*, *23*(5-6), 529–560. https://doi.org/10.1016/j.quascirev.2003.09.007

Kay, J. E., Holland, M. M., & Jahn, A. (2011). Inter-annual to multi-decadal Arctic Sea ice extent trends in a warming world. *Geophysical Research Letters*, *38*, L15708. https://doi.org/10.1029/2011GL048008

Khan, S. A., Kjær, K. H., Bevis, M., Bamber, J. L., Wahr, J., Kjeldsen, K. K., et al. (2014). Sustained mass loss of the northeast Greenland ice sheet triggered by regional warming. *Nature Climate Change*, *4*, 292.

Kjeldsen, K. K., Korsgaard, N. J., Bjørk, A. A., Khan, S. A., Box, J. E., Funder, S., et al. (2015). Spatial and temporal distribution of mass loss from the Greenland ice sheet since AD 1900. *Nature*, *528*(7582), 396–400. https://doi.org/10.1038/nature16183

Koç, N., Jansen, E., & Haflidason, H. (1993). Paleoceanographic reconstructions of surface ocean conditions in the Greenland, Iceland and Norwegian seas through the last 14 ka based on diatoms. *Quaternary Science Reviews*, *12*, 115–140. https://doi.org/10.1016/0277-,3791(93)90012-B

Kolling, H. M., Stein, R., Fahl, K., Perner, K., & Moros, M. (2017). Short-term variability in late Holocene sea ice cover on the East Greenland shelf and its driving mechanisms. *Palaeogeography Palaeoclimatology Palaeoecology*, *485*, 336–350. https://doi.org/10.1016/j.palaeo.2017.06.024

Köseoğlu, D., Belt, S. T., Husum, K., & Knies, J. (2018). An assessment of biomarker-based multivariate classification methods versus the PIP_{25} index for paleo Arctic Sea ice reconstruction. *Organic Geochemistry*, *125*, 82–94. https://doi.org/10.1016/j.orggeochem.2018.08.014

Köseoğlu, D., Belt, S. T., Smik, L., Yao, H., Panieri, G., & Knies, J. (2018). Complementary biomarker-based methods for characterising Arctic sea ice conditions: A case study comparison between multivariate analysis and the PIP_{25} index. *Geochimica et Cosmochimica Acta*, *222*, 406–420. https://doi.org/10.1016/j.gca.2017.11.001

Krieger, L., Floricioiu, D., & Neckel, N. (2020). Drainage basin delineation for outlet glaciers of Northeast Greenland based on Sentinel-1 ice velocities and TanDEM-X elevations. *Remote Sensing of Environment*, *237*, 111483. https://doi.org/10.1016/j.rse.2019.111483

Krumpen, T., Belter, H. J., Boetius, A., Damm, E., Haas, C., Hendricks, S., et al. (2019). Arctic warming interrupts the transpolar drift and affects long-range transport of sea ice and ice-rafted matter. *Scientific Reports*, *9*(1), 5459. https://doi.org/10.1038/s41598-019-41456-y

Larsen, N. K., Levy, L. B., Carlson, A. E., Buizert, C., Olsen, J., Strunk, A., et al. (2018). Instability of the Northeast Greenland ice stream over the last 45,000 years. *Nature Communications*, *9*(1), 1872. https://doi.org/10.1038/s41467-018-04312-7

Laskar, J., Robutel, P., Joutel, F., Gastineau, M., Correia, A. C. M., & Levrard, B. (2004). A long-term numerical solution for the insolation quantities of the Earth. *Astronomy & Astrophysics*, *428*(1), 261–285. https://doi.org/10.1051/0004-6361:20041335

Leventer, A. (2013). The fate of Antarctic "Sea Ice Diatoms" and their use as paleoenvironmental indicators. In M. P. Lizotte, & K. R. Arrigo (Eds.), *Antarctic sea ice: Biological processes, interactions and variability*, *AGU research series 73* (pp. 121–137). Washington, D.C: AGU.

Limoges, A., Massé, G., Weckström, K., Poulin, M., Ellegaard, N., Heikkilä, M., et al. (2018). Spring succession and vertical export of diatoms and IP_{25} in a seasonally ice-covered high Arctic fjord. *Frontiers in Earth Science*, *6*, 226. http://doi.org/10.3389/feart.2018.00226

MacGregor, J. A., Colgan, W. T., Fahnestock, M. A., Morlighem, M., Catania, G. A., Paden, J. D., & Gogineni, S. P. (2016). Holocene deceleration of the Greenland ice sheet. *Science*, *351*, 590–593. https://doi.org/10.1126/science.aab1702

Maslanik, J. A., Fowler, C., Stroeve, J., Drobot, S., Zwally, J., Yi, D., & Emery, W. (2007). A younger, thinner Arctic ice cover: Increased potential for rapid, extensive sea-ice loss. *Geophysical Research Letters*, *34*, L24501. https://doi.org/10.1029/2007GL032043

Mayer, C., Reeh, N., Jung-Rothenhäusler, F., Huybrechts, P., & Oerter, H. (2000). The subglacial cavity and implied dynamics under Nioghalvfjerdsfjorden glacier, NE-Greenland. *Geophysical Research Letters*, *27*(15), 2289–2292. https://doi.org/10.1029/2000GL011514

Mayer, C., Schaffer, J., Hattermann, T., Floricioiu, D., Krieger, L., Dodd, P. A., et al. (2018). Large ice loss variability at Nioghalvfjerdsfjorden glacier, Northeast-Greenland. *Nature Communications*, *9*(1), 2768. https://doi.org/10.1038/s41467-018-05180-x

McGregor, H. V., Evans, M. N., Goosse, H., Leduc, G., Martrat, B., Addison, J. A., et al. (2015). Robust global ocean cooling trend for the pre-industrial common era. *Nature Geoscience*, *8*, 671.

McKay, N. P., Kaufman, D. S., Routson, C. C., Erb, M. P., & Zander, P. D. (2018). The onset and rate of Holocene neoglacial cooling in the Arctic. *Geophysical Research Letters*, *45*, 12,487–12,496. https://doi.org/10.1029/2018GL079773

Meredith, M., Sommerkorn, M., Cassotta, S., Derksen, C., Ekaykin, A., Hollowed, A., et al. (2019). Polar regions. In *IPCC special report on the ocean and cryosphere in a changing climate*. IPCC Report.

Mote, T. L. (2007). Greenland surface melt trends 1973–2007: Evidence of a large increase in 2007. *Geophysical Research Letters*, *34*, L22507. https://doi.org/10.1029/2007GL031976

Mouginot, J., Rignot, E., Bjørk, A. A., van den Broeke, M., Millan, R., Morlighem, M., et al. (2019). Forty-six years of Greenland ice sheet mass balance from 1972 to 2018. *Proceedings of the National Academy of Sciences*, *116*(19), 9239–9244. https://doi.org/10.1073/pnas.1904242116

Mouginot, J., Rignot, E., Scheuchl, B., Fenty, I., Khazendar, A., Morlighem, M., et al. (2015). Fast retreat of Zachariæ Isstrøm, Northeast Greenland. *Science*, *350*, 1357–1361. https://doi.org/10.1126/science.aac7111

Müller, J., Massé, G., Stein, R., & Belt, S. T. (2009). Variability of sea-ice conditions in the Fram Strait over the past 30,000 years. *Nature Geoscience*, *2*(11), 772–776. https://doi.org/10.1038/ngeo665

Müller, J., Wagner, A., Fahl, K., Stein, R., Prange, M., & Lohmann, G. (2011). Towards quantitative sea ice reconstructions in the northern North Atlantic: A combined biomarker and numerical modelling approach. *Earth and Planetary Science Letters*, *306*(3-4), 137–148. https://doi.org/10.1016/j.epsl.2011.04.011

Müller, J., Werner, K., Stein, R., Fahl, K., Moros, M., & Jansen, E. (2012). Holocene cooling culminates in sea ice oscillations in Fram Strait. *Quaternary Science Reviews*, *47*, 1–14. https://doi.org/10.1016/j.quascirev.2012.04.024

Nam, S.-I., Stein, R., Grobe, H., & Hubberten, H. (1995). Late Quaternary glacial-interglacial changes in sediment composition at the East Greenland continental margin and their paleoceanographic implications. *Marine Geology*, *122*(3), 243–262. https://doi.org/10.1016/0025-3227(94)00070-2

NASA Worldview. (2019). https://worldview.earthdata.nasa.gov/, part of the NASA Earth Observing System Data and Information System (EOSDIS)

Nick, F. M., Vieli, A., Howat, I. M., & Joughin, I. (2009). Large-scale changes in Greenland outlet glacier dynamics triggered at the terminus. *Nature Geoscience*, *2*(2), 110–114. https://doi.org/10.1038/ngeo394

Nordhaus, W. (2019). Economics of the disintegration of the Greenland ice sheet. *Proceedings of the National Academy of Sciences*, *116*(25), 12,261–12,269. https://doi.org/10.1073/pnas.1814990116

Notz, D., & Marotzke, J. (2012). Observations reveal external driver for Arctic sea-ice retreat. *Geophysical Research Letters*, *39*, L08502. https://doi.org/10.1029/2012GL051094

Notz, D., & Stroeve, J. (2016). Observed Arctic sea-ice loss directly follows anthropogenic CO_2 emission. *Science*, *354*(6313), 747–750. https://doi.org/10.1126/science.aag2345

Parker, W. R., & Sills, G. C. (1990). Observation of corer penetration and sample entry during gravity coring. *Marine Geophysical Researches*, *12*(1-2), 101–107. https://doi.org/10.1007/BF00310566

Parkinson, C. L., & Cavalieri, D. J. (2008). Arctic sea ice variability and trends, 1979–2006. *Journal of Geophysical Research*, *113*, C07003. https://doi.org/10.1029/2007JC004558

Perner, K., Moros, M., Lloyd, J. M., Jansen, E., & Stein, R. (2015). Mid to Late Holocene strengthening of the East Greenland current paralleled by increased Atlantic intermediate water outflow from the Arctic Ocean. *Quaternary Science Reviews*, *129*, 296–307. https://doi.org/10.1016/j.quascirev.2015.10.007

Ran, L., Jiang, H., Knudsen, K. L., Eiríksson, J., & Gu, Z. (2006). Diatom response to the Holocene climatic optimum on the North Icelandic shelf. *Marine Micropaleontology*, *60*(3), 226–241. https://doi.org/10.1016/j.marmicro.2006.05.002

Reeh, N. (2004). Holocene climate and fjord glaciations in Northeast Greenland: Implications for IRD deposition in the North Atlantic. *Sedimentary Geology*, *165*(3-4), 333–342. https://doi.org/10.1016/j.sedgeo.2003.11.023

Reeh, N., Thomsen, H., Higgins, A., & Weidick, A. (2001). Sea ice and the stability of north and Northeast Greenland floating glaciers. *Annals of Glaciology*, *33*, 474–480. https://doi.org/10.3189/172756401781818554

Reimer, P. J., Bard, E., Bayliss, A., Beck, J. W., Blackwell, P. G., Ramsey, C. B., et al. (2013). IntCal13 and Marine13 radiocarbon age calibration curves 0–50,000 years cal BP. *Radiocarbon*, *55*(4), 1869–1887. https://doi.org/10.2458/azu_js_rc.55.16947

Ribeiro, S., Sejr, M. K., Limoges, A., Heikkilä, M., Andersen, T. J., Tallberg, P., et al. (2017). Sea ice and primary production proxies in surface sediments from a high Arctic Greenland fjord: Spatial distribution and implications for palaeoenvironmental studies. *Ambio*, *46*(S1), 106–118. https://doi.org/10.1007/s13280-016-0894-2

Rignot, E., & Kanagaratnam, P. (2006). Changes in the velocity structure of the Greenland ice sheet. *Science*, *311*, 986–990. https://doi.org/10.1126/science.1121381

Rignot, E., & Mouginot, J. (2012). Ice flow in Greenland for the international polar year 2008–2009. *Geophysical Research Letters*, *39*, L11501. https://doi.org/10.1029/2012GL051634

Rignot, E. J., Gogineni, S. P., Krabill, W. B., & Ekholm, S. (1997). North and Northeast Greenland ice discharge from satellite radar interferometry. *Science*, *276*, 934–937. https://doi.org/10.1126/science.276.5314.934

Rimbu, N., Lohmann, G., Kim, J.-H., Arz, H. W., & Schneider, R. (2003). Arctic/North Atlantic oscillation signature in Holocene Sea surface temperature trends as obtained from alkenone data. *Geophysical Research Letters*, *30*(6), 1280. https://doi.org/10.1029/2002GL016570

Rontani, J., Charrière, B., Sempéré, R., Doxaran, D., Vaultier, F., Vonk, J. E., & Volkman, J. K. (2014). Degradation of sterols and terrigenous organic matter in waters of the Mackenzie shelf, Canadian Arctic. *Organic Geochemistry*, *75*, 61–73.

Rontani, J.-F., Belt, S. T., & Amiraux, R. (2018). Biotic and abiotic degradation of the sea ice diatom biomarker IP25 and selected algal sterols in near-surface Arctic sediments. *Organic Geochemistry*, *118*, 73–88. https://doi.org/10.1016/j.orggeochem.2018.01.003

Ryan, W. B. F., Carbotte, S. M., Coplan, J. O., O'Hara, S., Melkonian, A., Arko, R., et al. (2009). Global multi-resolution topography synthesis. *Geochemistry, Geophysics, Geosystems*, *10*, Q03014. https://doi.org/10.1029/2008GC002332

Sasgen, I., van den Broeke, M., Bamber, J. L., Rignot, E., Sørensen, L. S., Wouters, B., et al. (2012). Timing and origin of recent regional ice-mass loss in Greenland. *Earth and Planetary Science Letters*, *333–334*, 293–303. https://doi.org/10.1016/j.epsl.2012.03.033

Schaffer, J., Kanzow, T., von Appen, W.-J., von Albedyll, L., Arndt, J. E., & Roberts, D. H. (2020). Bathymetry constrains ocean heat supply to Greenland's largest glacier tongue. *Nature Geoscience*, *13*(3), 227–231. https://doi.org/10.1038/s41561-019-0529-x

Schlitzer, R. (2018). Ocean data view, https://odv.awi.de

Schneider, W., & Budéus, G. (1994). The North East Water polynya (Greenland Sea). *Polar Biology*, *14*(1), 1–9. https://doi.org/10.1007/BF00240265

Schneider, W., & Budéus, G. (1997). Summary of the Northeast Water Polynya formation and development (Greenland Sea). *Journal of Marine Systems*, *10*(1–4), 107–122. https://doi.org/10.1016/S0924-7963(96)00075-9

Seale, A., Christoffersen, P., Mugford, R. I., & O'Leary, M. (2011). Ocean forcing of the Greenland ice sheet: Calving fronts and patterns of retreat identified by automatic satellite monitoring of eastern outlet glaciers. *Journal of Geophysical Research*, *116*, F03013. https://doi.org/10.1029/2010JF001847

Seroussi, H., Morlighem, M., Rignot, E., Larour, E., Aubry, D., Ben Dhia, H., & Kristensen, S. S. (2011). Ice flux divergence anomalies on 79 North Glacier, Greenland. *Geophysical Research Letters*, *38*, L09501. https://doi.org/10.1029/2011GL047338

Shepherd, A., Ivins, E., Rignot, E., Smith, B., van den Broeke, M., Velicogna, I., et al. (2020). Mass balance of the Greenland ice sheet from 1992 to 2018. *Nature*, *579*(7798), 233–239. https://doi.org/10.1038/s41586-019-1855-2

Smedsrud, L. H., Halvorsen, M. H., Stroeve, J.C., Zhang, R., & Kloster, K. (2017). Fram Strait sea ice export variability and September Arctic sea ice extent over the last 80 years. *The Cryosphere*, *11*, 65–79.

Smik, L., Cabedo-sanz, P., & Belt, S. T. (2016). Organic geochemistry semi-quantitative estimates of paleo Arctic sea ice concentration based on source-specific highly branched isoprenoid alkenes: A further development of the PIP_{25} index. *Organic Geochemistry*, *92*, 63–69. https://doi.org/10.1016/j.orggeochem.2015.12.007

Sneed, W. A., & Hamilton, G. S. (2016). Recent changes in the Norske Øer ice barrier, coastal Northeast Greenland. *Annals of Glaciology*, *57*(73), 47–55. https://doi.org/10.1017/aog.2016.21

Stein, R. (2008). *Arctic Ocean sediments: processes, proxies, and paleoenvironment*. Amsterdam: Elsevier.

Stein, R., & Fahl, K. (2012). A first southern Lomonosov ridge (Arctic Ocean) 60 ka IP_{25} sea-ice record. *Polarforschung*, *82*, 83–86.

Stein, R., Fahl, K., Gierz, P., Niessen, F., & Lohmann, G. (2017). Arctic Ocean sea ice cover during the penultimate glacial and the last interglacial. *Nature Communications*, *8*(1), 373. https://doi.org/10.1038/s41467-017-00552-1

Stein, R., Fahl, K., Schreck, M., Knorr, G., Niessen, F., Forwick, M., et al. (2016). Evidence for ice-free summers in the late Miocene Central Arctic Ocean. *Nature Communications*, *7*, 11148.

Stein, R., Grobe, H., Hubberten, H., Marienfeld, P., & Nam, S. (1993). Latest Pleistocene to Holocene changes in glaciomarine sedimentation in Scoresby Sund and along the adjacent East Greenland continental margin: Preliminary results. *Geo-Marine Letters*, *13*(1), 9–16. https://doi.org/10.1007/BF01204387

Stein, R., & Macdonald, R. W. (2004). Geochemical proxies used for organic carbon source identification in Arctic Ocean sediments. In R. Stein, & R. W. Macdonald (Eds.), *The organic carbon cycle in the Arctic Ocean* (pp. 24–30). Berlin: Springer-Verlag. https://doi.org/10.1007/978-3-642-18912-8_7

Stein, R., Nam, S., Grobe, H., & Hubberton, H. (1996). Late Quaternary glacial history and short-term ice-rafted debris fluctuations along the East Greenland continental margin. *Geological Society, London, Special Publications*, *111*, 135–151. https://doi.org/10.1144/GSL.SP.1996.111.01.09

Stern, N., & Taylor, C. (2007). Climate change: Risk, ethics, and the Stern review. *Science*, *317*, 203–204. https://doi.org/10.1126/science.1142920

Straneo, F., & Cenedese, C. (2015). The dynamics of Greenland's glacial fjords and their role in climate. *Annual Review of Marine Science*, *7*(1), 89–112. https://doi.org/10.1146/annurev-marine-010213-135133

Straneo, F., Sutherland, D. A., Holland, D., Gladish, C., Hamilton, G. S., Johnson, H. L., et al. (2012). Characteristics of ocean waters reaching Greenland' s glaciers. *Annals of Glaciology*, *53*(60), 202–210. https://doi.org/10.3189/2012AoG60A059

Stroeve, J., Holland, M. M., Meier, W., Scambos, T., & Serreze, M. (2007). Arctic Sea ice decline: Faster than forecast. *Geophysical Research Letters*, *34*, L09501. https://doi.org/10.1029/2007GL029703

Stuiver, M. Reimer, P. J. Reimer, R.W. (2019). CALIB 7.1 [WWW program] at http://calib.org

Syring, N., Stein, R., Fahl, K., Vahlenkamp, M., Zehnich, M., Spielhagen, R. F., & Niessen, F. (2020). Holocene changes in sea-ice cover and polynya formation along the eastern North Greenland shelf: New insights from biomarker records. *Quaternary Science Reviews*, *231*, 106173. https://doi.org/10.1016/j.quascirev.2020.106173

Tedesco, M. (2007). A new record in 2007 for melting in Greenland. *Eos Transactions American Geophysical Union*, *88*, 383. https://doi.org/10.1029/2007EO390003

Thackeray, C. W., & Hall, A. (2019). An emergent constraint on future Arctic Sea-ice albedo feedback. *Nature Climate Change*, *9*(12), 972–978. https://doi.org/10.1038/s41558-019-0619-1

Thomas, R., Frederick, E., Krabill, W., Manizade, S., & Martin, C. (2009). Recent changes on Greenland outlet glaciers. *Journal of Glaciology*, *55*(189), 147–162. https://doi.org/10.3189/002214309788608958

Topp, R., & Johnson, M. (1997). Winter intensification and water mass evolution from yearlong current meters in the Northeast Water Polynya. *Journal of Marine Systems*, *10*(1-4), 157–173. https://doi.org/10.1016/S0924-7963(96)00083-8

van den Broeke, M., Bamber, J., Ettema, J., Rignot, E., Schrama, E., van de Berg, W. J., et al. (2009). Partitioning recent Greenland mass loss. *Science*, *326*, 984–986. https://doi.org/10.1126/science.1178176

Volkman, J. K. (1986). A review of sterol markers for marine and terrigenous organic matter. *Organic Geochemistry*, *9*(2), 83–99. https://doi.org/10.1016/0146-6380(86)90089-6

Volkman, J. K., Barrett, S. M., Dunstan, G. A., & Jeffrey, S. W. (1993). Geochemical significance of the occurrence of dinosterol and other 4-methyl sterols in a marine diatom. *Organic Geochemistry*, *20*(1), 7–15. https://doi.org/10.1016/0146-6380(93)90076-N

Volkman, J. K., Revill, A. T., Holdsworth, D. G., & Fredericks, D. (2008). Organic matter sources in an enclosed coastal inlet assessed using lipid biomarkers and stable isotopes. *Organic Geochemistry*, *39*(6), 689–710. https://doi.org/10.1016/j.orggeochem.2008.02.014

Vonmoos, M., Beer, J., & Muscheler, R. (2006). Large variations in Holocene solar activity: Constraints from ^{10}Be in the Greenland ice core project ice core. *Journal of Geophysical Research*, *111*, A10105. https://doi.org/10.1029/2005JA011500

Werner, K., Müller, J., Husum, K., Spielhagen, R. F., Kandiano, E. S., & Polyak, L. (2016). Holocene Sea subsurface and surface water masses in the Fram Strait—Comparisons of temperature and sea-ice reconstructions. *Quaternary Science Reviews*, *147*, 194–209. https://doi.org/10.1016/j.quascirev.2015.09.007

Wilson, N. J., & Straneo, F. (2015). Water exchange between the continental shelf and the cavity beneath Nioghalvfjerdsbræ (79 north glacier). *Geophysical Research Letters*, *42*, 7648–7654. https://doi.org/10.1002/2015GL064944

Winkelmann, D., Jokat, W., Jensen, L., & Schenke, H. W. (2010). Submarine end moraines on the continental shelf off NE Greenland - implications for Lateglacial dynamics. *Quaternary Science Reviews*, *29*(9–10), 1069–1077. https://doi.org/10.1016/j.quascirev.2010.02.002

Wollenburg, J. E., & Mackensen, A. (1998). Living benthic foraminifera from the Central Arctic Ocean: Faunal composition, standing stock and diversity. *Marine Micropaleontology*, *34*(3–4), 153–185. https://doi.org/10.1016/S0377-8398(98)00007-3

Xiao, X., Zhao, M., Knudsen, K. L., Sha, L., Eiríksson, J., Gudmundsdóttir, E., et al. (2017). Deglacial and Holocene sea-ce variability north of Iceland and response to ocean circulation changes. *Earth and Planetary Science Letters*, *472*, 14–24. https://doi.org/10.1016/j.epsl.2017.05.006

Yunker, M. B., Macdonald, R. W., Veltkamp, D. J., & Cretney, W. J. (1995). Terrestrial and marine biomarkers in a seasonally ice-covered Arctic estuary—Integration of multivariate and biomarker approaches. *Marine Chemistry*, *49*(1), 1–50. https://doi.org/10.1016/0304-4203(94)00057-K

Zehnich, M., Spielhagen, R. F., Bauch, H. A., Forwick, M., Hass, H. C., Palme, T., et al. (2020). Environmental variability off NE Greenland (western Fram Strait) during the past 10,600 years. *The Holocene*, *30*(12), 1752–1766. https://doi.org/10.1177/0959683620950393